Dissecting the polar dichotomy of the noncondensable gas enhancement on Mars using the NASA Ames Mars General Circulation Model

Steven M. Nelli,[1,2] James R. Murphy,[2] Ann L. Sprague,[3] William V. Boynton,[3] Kris E. Kerry,[3] Daniel M. Janes,[3] and Albert E. Metzger[4,5]

Received 20 October 2006; revised 29 March 2007; accepted 29 May 2007; published 25 August 2007.

[1] The atmospheric processes underlying the observed spatial and temporal enhancement of noncondensing gases in Mars' atmosphere are investigated. The Gamma Ray Spectrometer (GRS) on board Mars Odyssey has obtained measurements indicating that the absolute and relative column abundance of noncondensing gases (primarily argon and nitrogen) maximizes at high latitudes in both hemispheres during winter as CO_2 gas condenses and forms the seasonal polar ice cap. This condensing CO_2 "leaves behind" noncondensing gases whose local absolute and relative column abundances can increase at a rate controlled by mixing with less-enhanced air from lower latitudes. Understanding the processes responsible for the magnitude and seasonal variations of these enhancement values is an aid in understanding atmospheric transport processes. The NASA Ames Mars General Circulation Model is employed to help understand the atmospheric thermodynamical mechanisms that give rise to the observed temporal and magnitude variations in the polar enhancement values. The model produces a threefold noncondensable gas enhancement in the south polar region and an approximate 1.4-fold increase in noncondensables in the north polar region. These model results are temporally consistent with observed values, but the observed enhancement magnitudes exceed those modeled by up to a factor of two. The difference in strength and the season of formation between transient eddies in the southern and northern hemispheres may play a large role in determining the different character of the two polar enhancements. Model simulations also illuminate the effect that topography, orbital eccentricity, and atmospheric dust opacity have on producing the north versus south polar enhancement dichotomy.

Citation: Nelli, S., J. R. Murphy, A. L. Sprague, W. V. Boynton, K. E. Kerry, D. M. Janes, and A. E. Metzger (2007), Dissecting the polar dichotomy of the noncondensable gas enhancement on Mars using the NASA Ames Mars General Circulation Model, *J. Geophys. Res.*, *112*, E08S91, doi:10.1029/2006JE002849.

1. Introduction

[2] The direct condensation of Mars' main atmospheric component (CO_2) has no terrestrial analogue. As much as 30% of the atmospheric mass condenses out on to Mars' seasonal polar ice caps [*Forget*, 2004]. On the basis of Viking Lander 2 measurements [*Owen et al.*, 1977], nominal abundances for gaseous species on Mars are 95.3% CO_2 and 4.7% noncondensable gases (2.7% nitrogen, 1.6% argon, and traces of others), but the condensation of CO_2 over the Martian poles "leaves behind," within the atmosphere, noncondensing gases, resulting in an increase in their local absolute and relative abundances. The magnitude of this increase in abundance, hereafter referred to as enhancement (further defined in section 6), is dependent upon the quantity of CO_2 condensed and upon latitudinal mixing with lower-latitude air. Previous work has speculated that reduced CO_2 partial pressure within an enhanced noncondensable gas abundance could result in depressed brightness temperatures measured by the Viking and Mars Global Surveyor orbiters [*Kieffer et al.*, 1976, 1977; *Weiss and Ingersoll*, 2000]. The magnitude of the argon gas enhancement over both Martian winter poles has been quantified via analysis of measurements obtained with the Gamma Ray Spectrometer (GRS) on board the Mars Odyssey orbiter spacecraft [*Prettyman et al.*, 2004; *Sprague et al.*, 2004, 2007].

[3] The mixing ratio (gm/gm) of noncondensable gases is a function of the column mass of noncondensables (g cm^{-2})

[1]Department of Atmospheric, Oceanic, and Space Sciences, University of Michigan, Ann Arbor, Michigan, USA.
[2]Department of Astronomy, New Mexico State University, Las Cruces, New Mexico, USA.
[3]Lunar and Planetary Laboratory, University of Arizona, Tucson, Arizona, USA.
[4]Jet Propulsion Laboratory, Pasadena, California, USA.
[5]California Institute of Technology, Pasadena, California, USA.

0148-0227/07/2006JE002849

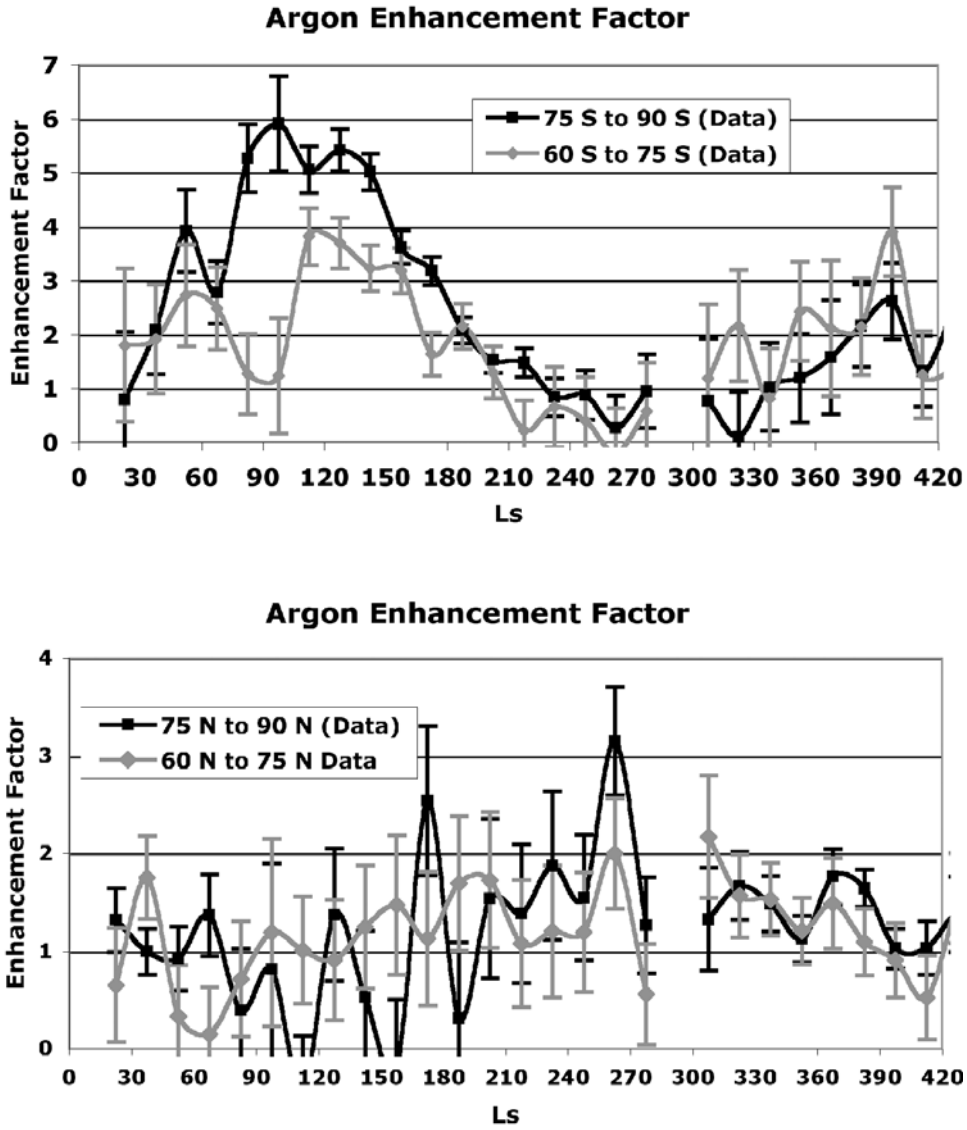

Figure 1. Seasonally varying Mars Odyssey orbiter gamma-sensor-derived zonal mean column integrated argon enhancement factor at the indicated latitudes, relative to Viking Lander 2 GCMS-derived argon abundance (mixing ratio) at $L_s = 135°$. Figure reproduced from *Sprague et al.* [2007].

and of the column mass of CO_2 (g cm^{-2}). In this paper, it is the local change in the mixing ratio of noncondensable gases that is of interest. The local changes in noncondensable gas mixing ratio arise due to the CO_2 condensation/sublimation in a column (increasing/decreasing the local noncondensable gas mixing ratio), and to the subsequent development of circulations responding to the changes in the pressure field producing the transport of additional noncondensable gases into/out the column. The noncondensable gas mixing ratio of 4.7% measured at the Viking Lander 2 site [*Owen et al.*, 1977] provides the standard against which noncondensable gas abundance is defined. Throughout this paper, we employ the term enhancement (or enrichment) of noncondensable gas to indicate when the total amount (g cm^{-2}) of noncondensable gas in the column exceeds the amount that would be expected for a column experiencing the measured Viking Lander 2 noncondensable gas mixing ratio. Since the peak enhancement magnitudes experienced (1.5–6) exceed the greatest temporal variation (~1.3) in CO_2 column abundance, the enhancement value, while being a relative measure, also provides information about the absolute column abundance of noncondensable gases. A full description of how the noncondensable gas enhancement is defined for the data and model results is contained in section 6.

[4] More than one Martian year of atmospheric argon measurements from the 2001 Mars Odyssey GRS have been reduced for analysis [*Sprague et al.*, 2007]. The data investigated in this paper commence when GRS began mapping, $L_s = 21.95°$ (June 2002) and end with data taken at $L_s = 60°$ (November 2004) the following Mars year (~1.1 Mars years later). Of particular interest in these data are the enhanced absolute and relative column abundances of atmospheric argon at polar latitudes during the winter season compared to the observed atmospheric argon abundance at lower latitudes (Figure 1). The GRS data indicate a

sixfold enhancement in argon column abundance at the south pole and a threefold enhancement at the north pole [*Sprague et al.*, 2004, 2007] compared to argon mixing ratio values measured with the Viking Lander 2 (VL2) Gas Chromatograph Mass Spectrometer (GCMS) at northern middle latitudes during northern summer [*Owen et al.*, 1977]. When considering the quantity of CO_2 condensed, the noncondensable gas enhancement over both poles would be greater than what is currently observed if all noncondensable gas remained above the seasonal cap, suggesting that atmospheric transport to lower latitudes also must be considered [*Sprague et al.*, 2004]. Under the assumption that noncondensable gases are considered to be well mixed with respect to one another, and since there are no known sources or sinks of these gases on short (decadal) timescales, the remainder of this paper will assume the observed enhancement in argon to be equivalent to an enhancement in all noncondensable gases. This lack of sources and sinks of noncondensable gases also results in these gases serving as effective passive tracers of the atmospheric circulation, since only CO_2 sublimation and condensation and transport within the atmosphere affect the local noncondensable abundance (mixing ratio). We will exploit this passive tracer nature of the noncondensable gases to investigate the atmospheric circulation components that play a role in the magnitude of polar enhancement during seasonal cap growth.

[5] The NASA Ames General Circulation Model (GCM) permits the investigation of the thermodynamic processes related to the observed noncondensable gas enhancements. This model allows for the determination of the factors controlling the characteristic differences between the south and north polar enhancements. Comparison of the data to model results explores deficiencies in the Ames GCM ability to capture the atmospheric dynamics and transport processes. Here we present numerical modeling that investigates both the atmospheric circulation components and their responses to relevant forcing mechanisms (i.e., surface properties, atmospheric dust loads, etc.); their study leads to insight on how noncondensable gas enhancements may have been effected in prior Martian epochs. The results obtained aid in the interpretation of the GRS noncondensable gas abundance results and also help to illustrate differences in winter atmosphere dynamics between the high northern and high southern Martian latitudes.

[6] Section 2 provides a brief history of the issues related to noncondensable gas enhancement over the winter poles. In section 3, the GRS data used for comparison with the model are outlined. Section 4 provides a description of the NASA Ames General Circulation Model used in this effort. Section 5 outlines the community's current knowledge of Martian atmospheric transport. In section 6, a summary of the results from the various simulations is presented, and section 7 is a discussion of the conclusions drawn from this work and the implications this work has on prior Martian epochs.

2. Historical Perspective

[7] The Infrared Thermal Mapper (IRTM) instrument on board the Viking Orbiters of the 1970s recorded 20 μm surface brightness temperatures (T20) of $\sim$133 Kelvin over the south pole. Such temperatures were well below the expected saturation temperature of $\sim$150 Kelvin consistent with a surface partial pressure of CO_2 of $\sim$6 millibars [*Kieffer et al.*, 1976, 1977; *Snyder*, 1979]. These IRTM measurements were puzzling, especially since they were much lower than measurements obtained by the infrared radiometers and spectrometers on board Mariners 7 and 9 [*Neugebauer et al.*, 1971; *Hanel et al.*, 1972; *Kieffer et al.*, 1976]. These two Mariner missions recorded south polar temperatures of $\sim$148 K, although neither mission returned data during the southern polar night [*Kieffer et al.*, 1976].

[8] Between $L_s = 130^\circ$ and the end of the Viking primary mission ($L_s = 151^\circ$), several south polar T20 cold temperature regions were detected [*Kieffer et al.*, 1977]. Temperatures were as low as 133 K in these prominent regions [*Kieffer et al.*, 1976, 1977; *Snyder*, 1979], while much of the rest of the cap had T20 temperatures close to 143 K [*Kieffer et al.*, 1977]. These prominent low-temperature features occurred between -68° and -82° latitude and in three of the four longitude quadrants. Only the quadrant centered on 225°W contained no prominent cold spots [*Kieffer et al.*, 1977].

[9] Two early explanations for the observed depressed surface brightness temperatures were proposed: IR scattering by clouds, or CO_2 depletion/condensation causing temperature depression at the base of the atmospheric column [*Kieffer et al.*, 1976, 1977]. Water clouds were not a factor; the atmosphere was very clear and very dry (the saturated mixing ratio was below 10^{-6} in the polar night) [*Kieffer et al.*, 1977]. CO_2 clouds raise the altitude from which the T20 radiation originates [*Kieffer et al.*, 1976, 1977], but temperatures measured at 0.63 mbars were 163 K, well above the frost point of CO_2 [*Kieffer et al.*, 1977]. While most of these cold spots lay within the polar night, making them impossible to photograph, it was possible to image a cold spot located at -72° latitude and 160°W on $L_s \sim 144^\circ$. Images were clear and sharp with no distinct cloud features poleward of -50 degrees. Images in the violet and red were nearly equal in contrast. Differences in these two filters are indicators of cloud features. There were no corresponding IRTM data of this region for this sequence of imaging. However, a minimum temperature of 137 K was measured at this location both on $L_s \sim 139^\circ$ and $L_s \sim 151^\circ$, suggesting this local minimum persisted throughout the primary mission [*Kieffer et al.*, 1977].

[10] As CO_2 condenses over the winter pole, noncondensables are left behind, the main constituents being Ar and N_2. The atmospheric response to the low-pressure region forming over the winter pole is to transport nondepleted air from lower latitudes into the winter polar region [*Haberle et al.*, 1993]. As long as the CO_2 vapor pressure is above the saturation vapor pressure, both CO_2 condensation and the noncondensable enrichment process will continue. The magnitude of noncondensable enhancement is dependent upon the rate of CO_2 condensation and on eddy mixing away from the pole [*Kieffer et al.*, 1977]. *Kieffer et al.* [1976] suggest that during southern hemisphere winter, the increase of noncondensables in the bottom 100 m of the atmosphere would be 16-fold (going from 5% to 80% of the total mass), lowering the CO_2 condensation temperature to 137 K from the expected 150 K at the south pole.

[11] Later, *Ditteon and Kieffer* [1979] concluded that improper emissivities were used to determine the temperature of the CO_2 ice. Previous values were assumed to be near unity. They condensed CO_2 in a low-temperature chamber and measured the formal range for the 20 μm band emissivity to be 0.62 to 0.89, with a best-estimated value of 0.72. Using the frost point temperature of 149 K and the lab-measured value for emissivity, the T20 brightness temperature would be 140 K. This temperature matches very well with the T20 measurement of 143 K across the whole of the larger south circumpolar region. The lowest lab value for emissivity (0.62) would produce a T20 temperature of 135 K, capable of explaining the measured brightness in the prominent cold spots. *Ditteon and Kieffer* [1979] concluded that the south pole does not require any drastic near-surface atmospheric compositional changes to account for the measured low surface brightness regions.

[12] The *Ditteon and Kieffer* [1979] value for the CO_2 emissivity is low compared to the best-fit parameter (emissivity = 0.85) from a simple polar heat-budget model of the Viking IRTM solar reflectance and infrared emission measurements [*James et al.*, 1992]. The calculated value of 80% noncondensable gas abundance by mass estimated by *Kieffer et al.* [1976] for the necessary temperature depression needs extraordinary conditions to occur (in order to prevent convection from transporting the noncondensable gas enhancement out of the polar region, a 100 km depleted column or a strong near-surface temperature inversion must be maintained) [*Weiss and Ingersoll*, 2000]. It is more likely that the T20 low brightness temperature phenomenon is due to a combination of low emissivity CO_2 ice and to the enhancement of noncondensable gases observed by the Mars Odyssey GRS instrument team [*Forget*, 2004]. Thus it becomes essential to understand the noncondensable gas cycle and to measure the amount of noncondensable gas so that one might determine how much of the brightness temperature depression is caused by this enrichment. In doing so, it may help to put an independently derived constraint on emissivity values in the south polar region. Even without constraining the emissivity of the seasonal CO_2 ice, the value of this work lies in the interpretation of the GRS data.

3. Data Description

[13] We are able to gain physical insights regarding the controlling factors of noncondensable accumulation and distribution in Mars' atmosphere by comparison of model results to observed Ar abundance. The data set was obtained with the Gamma Sensor (GS) of the Gamma Ray Spectrometer (GRS) on 2001 Mars Odyssey [*Boynton et al.*, 2004; W. V. Boynton et al., Data analysis of the GRS GS instrument, submitted to *Journal of Geophysical Research,* 2007]. The GS measures line emission at 1294 keV from gamma-ray (γ) decay of ^{41}Ar made from neutron capture by ^{40}Ar in the Martian atmosphere and from spallation of ^{48}Ti in the GS container. The data are zonally averaged (360° of longitude) over bins spanning 15° in latitude and 15° in aerocentric longitude of Mars in its orbit (L_s). The measurements are available from L_s = 22° of the first mapping year (June 2002) to L_s = 112° of the second mapping year (November 2004). After proper background subtraction [see *Sprague et al.*, 2007], the data are indicative of the amount of argon in Mars' atmosphere. A subset of these data (south polar data from L_s = 22° to L_s = 277°) were published previously [*Sprague et al.*, 2004]. In that paper, meridional eddy mixing coefficients were inferred for late autumn and throughout winter by using a simple model of advection and eddy transport of Ar into and out of the south polar region. The computations were based on the actual Mars atmospheric Ar measurements. A similar calculation using GCM results are compared to those of *Sprague et al.* [2004] in section 6.

[14] Here we use the entire data set for all latitudes and all available L_s to compare to our models of noncondensable gases and atmospheric transport. Atmospheric Ar between the spacecraft and the surface absorbs thermal neutrons coming from the atmosphere and the surface. The flux of neutrons varies with season due to the waxing and waning of the seasonal CO_2 frost cap. These seasonal variations are easily removed by taking the ratio of the emission line area of the 1294 keV line created by γ decay of ^{41}Ar made by neutron capture of ^{40}Ar in Mars' atmosphere (after subtraction of the component from ^{48}Ti spallation) to the peak area of the 1382 keV line area resulting from neutron capture of ^{48}Ti in the detector housing of the instrument. After the seasonal effects are removed, the data are calibrated to column mass abundance by using the ^{40}Ar mass mixing ratio (0.0145) measured by the gas chromatograph mass spectrometer on VL2 and our GCM computation of the column mass of the Mars atmosphere for the VL2 location and season. The data and details of the data reduction and analysis are presented in an accompanying article in this special section [*Sprague et al.*, 2007] and not discussed further here.

4. Model Description

[15] The NASA Ames Mars GCM (version 1.7.3) is a grid point (finite difference) numerical model for Mars' atmosphere originally derived from a terrestrial GCM [*Leovy and Mintz*, 1969]. Subsequent developments have included an improved treatment of radiative transfer, the inclusion of CO_2 condensation/sublimation, spatially variable lower boundary conditions (topography, thermal inertia, albedo), improved boundary layer treatment, aerosol transport, modified grid structure, and an improved dynamical core [*Pollack et al.*, 1990; *Murphy et al.*, 1995; *Suarez and Takacs*, 1995; *Haberle et al.*, 1999, 2003]. The surface topography is based on observations obtained by MOLA [*Smith et al.*, 1999], while thermal inertia and surface albedo fields employ Viking and Mars Global Surveyor observations (F. Forget, personal communication, 2005). The current model uses the Arakawa C-grid configuration. This configuration does not center a grid box over the pole, which in previous models led to excessive zonal wind speeds near the poles [*Murphy et al.*, 1995]. Temperature, pressure, and geopotential are calculated at the center of the box. The wind speed is calculated at grid box boundaries. The grid structure of the model employed herein yields 23 × 40 × 24 (latitude, longitude, vertical) points, providing global coverage of the planet at a horizontal resolution of 7.5° latitude and 9.0° longitude. One simulation is run at 4.0° latitude by 5.0° longitude (44 × 72 grid points) to test

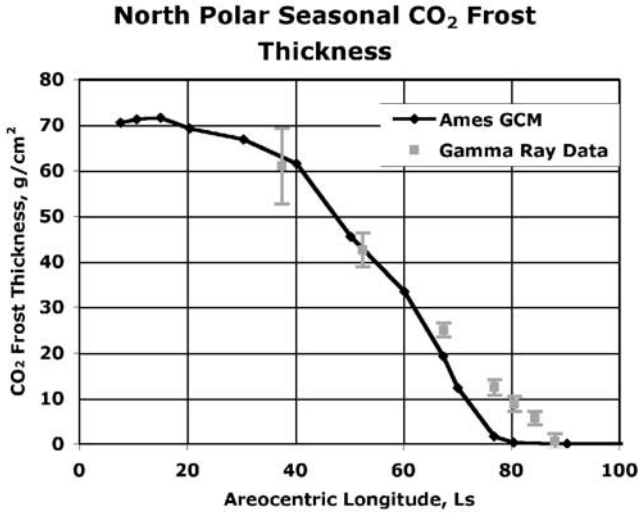

Figure 2. Seasonal CO_2 frost ice cap zonal mean column abundance (g/cm^2) at the north pole as a function of L_s. The connected diamonds are GCM-simulated values extrapolated to the pole. The squares are the inferred frost thickness based on the attenuation of 2.223 MeV gamma rays emitted by hydrogen [*Feldman et al.*, 2003]. Prior to $L_s = 35°$, the thickness of the CO_2 ice reduces the 2.223 MeV line strengths to a level too low for meaningful detection. Thickness for the south polar CO_2 frost cap has not yet been accurately determined from the GRS data.

the effects of spatial resolution upon the results. The top of the model atmosphere is bounded at the 0.0001 mbar level (~80 km). Model layer thickness increases with height, allowing for greater vertical resolution at the bottom of the atmosphere where dynamical instabilities are expected to be largest [*Haberle et al.*, 1982]. In calculating radiative heating rates, the model accounts for solar and thermal infrared absorption/re-emission by CO_2 and suspended dust [*Kahre et al.*, 2006]. The model includes the effects of diurnally and seasonally varying insolation, as well as the latent heat changes due to the deposition/sublimation of CO_2.

[16] For the results described below, we input into the model the values of dust opacity derived from MGS TES (Mars Global Surveyor Thermal Emission Spectrometer) spectra for mapping year 1 at the appropriate L_s. These MGS TES 9 μm opacity values [*Smith*, 2004] are temporally averaged over five degree L_s intervals (L_s = 0–5, 5–10, etc.) at the same horizontal resolution as the GCM. This remains true so long as half the TES data bins for a given latitude sampled contain information (empty bins are ignored in calculating the daily averaged opacity for a given latitude). As latitudes approach the polar night (where low signal-to-noise prevents reliable data retrieval), the likelihood of fewer than half the bins being filled with data increases. Upon reaching this arbitrary threshold, the opacity for this latitude becomes 70% the value of the adjacent equatorward latitude. Thus there is always a declining opacity toward the winter pole. The optical depth (twice the 9 μm opacity, as determined by *Martin* [1986] and *Clancy et al.* [2003]) at a model grid point for a specific L_s value (specific simulated sol) is determined via interpolation (in L_s space) between map values at that location and the two surrounding L_s values. The dust's vertical distribution varies spatially and temporally, being based upon *Conrath*'s [1975] prescription with a dependence upon the local column integrated optical depth (greater optical depth produces deeper dust mixing). For minimal dust loading (tau < 0.1), the mixing ratio at 1 scale height was ~50% of the surface value, while for opacity values greater than 0.85 the 50% mixing ratio level occurred 4.5 scale heights above the surface. These limits correspond to CONRATH parameter values of 0.4 (for the low-dust situation) and 0.007 (for the high-dust situation). The dust opacity affects the radiative heating rates in the model; this in turn affects the temperature, pressure and circulation.

[17] We initialize the model with a passive tracer (representing the noncondensing gas) in the form of a spatially uniform mixing ratio (mass of tracer divided by the total CO_2 mass in the grid box). CO_2 condenses at those locations where the local temperature is less than the CO_2 saturation temperature, which itself is based upon the local CO_2 gas pressure. Condensed CO_2 is assumed to immediately fall to the surface as "snow" in these initial simulations. It is not the removal of condensed CO_2, but the retention in the atmosphere of noncondensing gases, that produces the enhancements being investigated herein. The initial noncondensable gas mixing ratio is specified to be 4.7% on the basis of Viking Lander 2 GCMS measurements [*Owen et al.*, 1977]. A different value would change the absolute abundances discussed, but would not affect the relative enhancement values.

[18] The seasonal cap emissivity (0.38 in the south versus 0.62 in the north) for CO_2 ice in the model is not consistent with the laboratory-derived values obtained by *Ditteon and Kieffer* [1979]. The model values are used to reproduce the seasonal changes in atmospheric mass (atmospheric pressure) that matches the Viking Lander sites [*Tillman*, 1988]. The model emissivity values for each cap are essential for providing an appropriate CO_2 reservoir that matches observation. The Ames GCM does very well in producing the appropriate CO_2 reservoir and has heritage in doing so [*Murphy et al.*, 1995; *Haberle et al.*, 1999; *Feldman et al.*, 2005].

5. Atmospheric Transport

[19] To determine an upper limit for the noncondensable gas enhancement over each pole, the amount of CO_2 ice condensed over each pole in the model is used. Simulated north polar CO_2 deposition in the model (Figure 2) matches well with that derived at the north pole by the gamma ray and neutron spectrometer components of the GRS [*Feldman et al.*, 2003], removing concerns that the model has an improper reservoir. When looking at the condensed CO_2 near the poles as a function of season in the model, and assuming that for every 10 g/cm^2 of ice, 0.47 g/cm^2 of noncondensable gas is left behind, a maximum ninefold enhancement of noncondensable gas is predicted over the south polar region, with a maximum 3.5-fold enhancement predicted in the north (Figures 3 and 4). The disparity in the upper limit of the noncondensable gas enhancement between the two poles is due in large part to the factor of two difference in the CO_2 column abundance over each pole

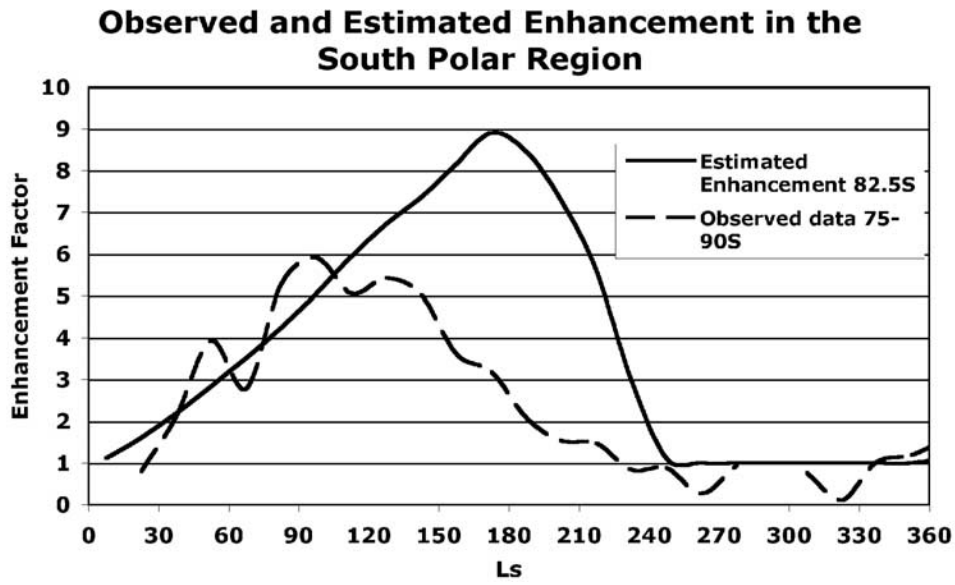

Figure 3. Mars Odyssey GRS-derived (black dashed line; same as the 82.5°S curve in Figure 1) zonal mean column integrated argon gas enhancement factor, and the predicted (black solid line) high southern latitude column integrated argon enhancement factor based solely upon the mass (g/cm^2) of GCM-simulated condensed CO_2.

(Figure 5). The larger amount of CO_2 ice deposition at the south pole over the north accounts for the rest of the difference between the upper limits of the noncondensable gas enhancements. From Figure 3 and 4, the enhancement factor calculated purely on the basis of CO_2 condensation is much greater than that observed (and is different in its growth and decline), suggesting the importance of atmospheric transport processes [*Sprague et al.*, 2004].

[20] The characteristic differences of the observed polar enhancements between the two poles seen in Figure 1 can be ascribed to transport processes. Condensation flow created by the formation and dissolution of the seasonal CO_2 ice caps produces circulation onto and off of the poles, respectively [*Haberle et al.*, 1993]. Condensation flow transports nondepleted air from lower latitudes into the fall/winter polar regions. This influx of noncondensable gases leads to the enhancing process. The explanation for why the enhancement fails to reach maximum noncondensable gas abundance according to CO_2 ice condensation and why the enhancement in the south develops with significant differences than that in the north is attributed to the behavior of the stationary and transient eddies, which act to transport mass away from the fall/winter poles.

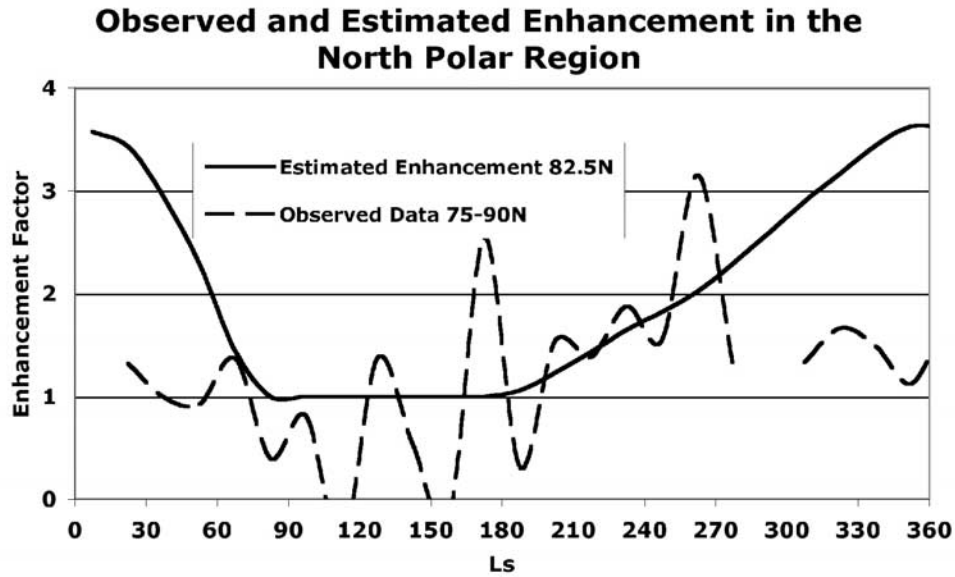

Figure 4. Same as Figure 3, except data are for the north polar region.

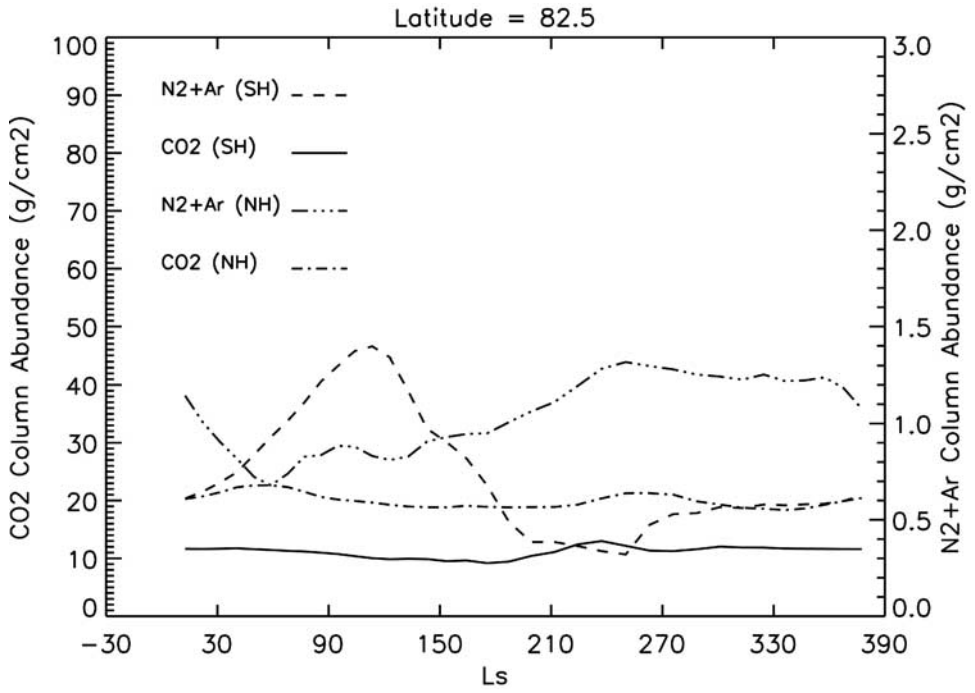

Figure 5. Time and zonal mean values of the GCM-simulated absolute atmospheric noncondensable and CO_2 column mass abundances (g/cm^2) for both 82.5°S (SH) and 82.5°N (NH) latitudes. The left axis corresponds to the CO_2 column abundance, and the right axis corresponds to noncondensable gas abundance. The maximum north and south polar noncondensable gas column abundances are nearly equal, but the increased atmospheric mass at the north pole reduces the relative abundance enhancement.

[21] Stationary waves manifest themselves as the presence of planetary waves that remain fixed in location relative to the underlying topography. These waves occur when the large-scale circulation, as well as thermal tides, passes over sizable topographic features. Stationary waves have their greatest influence in the upper atmosphere where they can cause sudden stratospheric warming. Analysis of TES data [*Banfield et al.*, 2003], as well as prior numerical studies [*Barnes et al.*, 1996; *Hollingsworth and Barnes*, 1996], details stationary waves as peaking in the winter hemisphere at 60° latitude. In both hemispheres, the amplitude of these waves is similar and thus is not expected to play a large role in defining the characteristic differences between the polar regions. Also, topographic relief poleward of 60° is uniform on scales needed to produce strong stationary waves, rendering the effects of stationary eddies in the polar regions innocuous.

[22] Transient eddies arise from instabilities in the large-scale wind and temperature fields produced by the differential heating between the equatorial and polar regions. Transient eddies are the storm systems that produce day-to-day variability in the weather. Analysis of MGS TES data finds that transient eddies peak in the fall and winter seasons with the eddy activity in the northern hemisphere being much more substantial than in the south [*Barnes*, 2006; *Banfield et al.*, 2004]. Typical periods for these storms are 2 to 30 sols [*Barnes*, 2006; *Banfield et al.*, 2004], with the maximum period still being about one half that of the high-frequency oscillations (changes in the magnitude of the enhancement over the course of 30° of L_s) seen in the observed northern hemisphere noncondensable gas enhancement. The origin of these oscillations is still in question. In the northern hemisphere, eddy activity peaks both in autumn and in middle winter. While in the south, eddy activity only peaks once near middle winter. The increased strength of the transient eddies in the northern hemisphere combined with their predilection to last throughout most of fall and winter may significantly reduce the enhancement of northern hemisphere noncondensable gases with respect to the south.

6. Results

[23] Model results are quantitatively and qualitatively compared to the data observed by Mars Odyssey GRS to assess the transport and CO_2 condensation physics of the model. A high-resolution simulation run at 4.0° by 5.0° (latitude × longitude) tests the effects that model resolution has on the results. We look at both the magnitude of the enhancement as well as the general circulation components between the 7.5° × 9.0° and the 4.0° × 5.0° simulations. We also study the significance, if any, that the high-latitude numerical filtering plays in the development of the polar enhancements.

6.1. Current Mars

[24] Using the NASA Ames GCM, the model is run with 7.5° by 9.0° (latitude versus longitude) spatial resolution, producing an annual pressure cycle representative of the Viking Lander 1 (VL1) measurements [*Tillman*, 1988] at the grid point nearest the VL1 location in the model. The model loses the last vestiges of the CO_2 frost more quickly than in

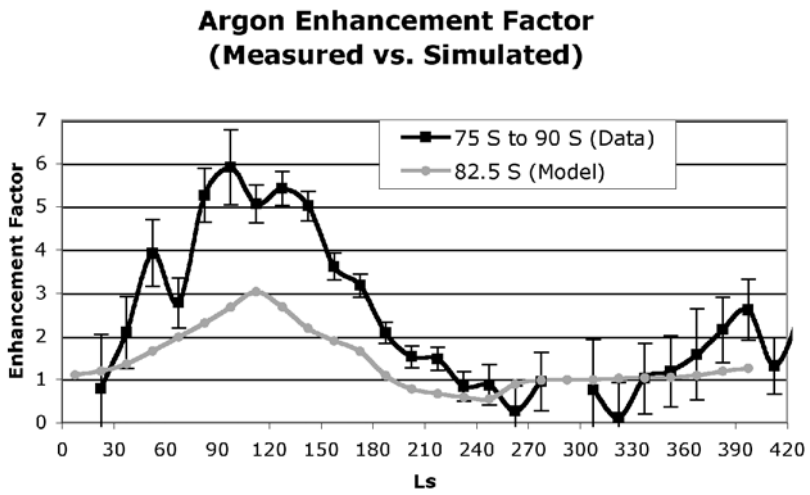

Figure 6. GCM-simulated (gray) and Mars Odyssey GRS-derived (black) zonal mean column integrated noncondensable gas enhancement at high southern latitudes. Values greater than unity indicate a relative abundance of noncondensable gases greater than detected in VL2 GCMS-measured abundances at L_s = 135° [*Owen et al.*, 1977], while enhancement values less than one indicate dilution (relative to VL2 GCMS abundances).

observation (Figure 2), but is otherwise a good fit. One note is that if the seasonal cap brightened in the late spring (unknown to date), this would slow down the regression of the seasonal cap. The model does not account for this. However, this is not of concern in regards to affecting the enhancement values in the model. The peak of the enhancement, both observed by GRS and modeled, occurs long before the seasonal CO_2 ice cap reaches full extent in either hemisphere. The surface pressure cycle at the grid point nearest the VL1 location is within a few tenths of a millibar of the observed pressure cycle [*Tillman*, 1988]. With the surface ice accumulation and the simulated pressure cycle near the VL1 position similar to that observed, there is confidence that the total amount of condensed CO_2 is appropriate and thus the modeled enhancement values are not being seriously affected by too little or too much CO_2 condensation.

[25] In Figures 6 and 7, the GCM-simulated enhancement of noncondensable gases at high northern and southern latitudes is presented along with the GRS-derived enhancement of noncondensable gases in the polar regions of Mars. For calculation of the GRS-derived enhancement and more detail on the binning described earlier, see *Sprague et al.* [2007] in this special section. To obtain the GCM enhancement values, we use the same method as *Sprague et al.* [2007]. We calculate the zonal mean values of both the CO_2 and noncondensable gas column abundance (g/cm^2) over bins of 15° L_s and 15° latitude (same bin size as for the GRS data). To obtain a "homogeneous" model (uniform mixing ratio) value of noncondensable gas column abundance, the gaseous CO_2 column abundance (g/cm^2) in each L_s and latitude bin is multiplied by 4.7% (the model-initiated value for noncondensable gas). The ratio of the simulated zonal mean noncondensable gas column abundance to the "homogeneous" zonal mean noncondensable gas column

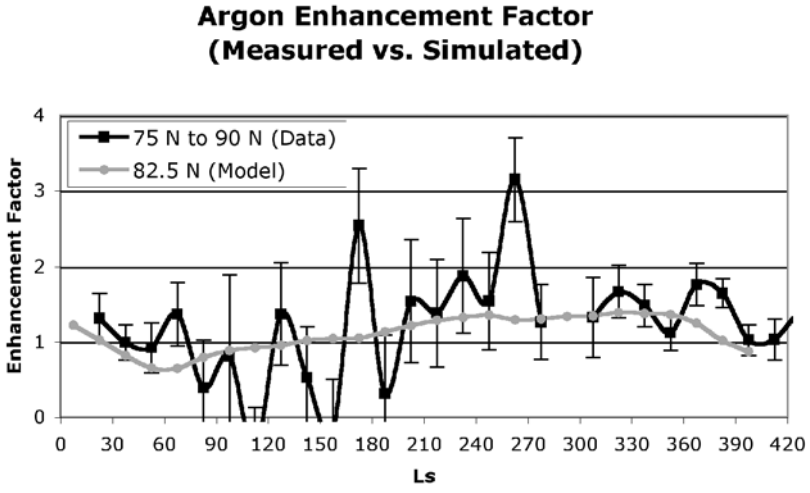

Figure 7. Same as Figure 6, but for high northern latitudes.

abundance then provides a quantitative measurement of the enhancement of the noncondensable gas. Ratio values greater than unity indicate an enhancement of noncondensable gases over that expected if the noncondensable gas were uniformly mixed at 4.7% atmospheric abundance. Values less than unity are depleted with respect to a uniformly mixed gas at 4.7% atmospheric abundance. Because the normalizing value comes from the location and time of the VL2 GCMS values, the yearly average enhancement will not be unity at the poles. Additionally, the changing total quantity of atmospheric mass through the year will itself produce variations as large as 30% in this "enhancement" value. This 30% factor could be minimized by accounting for the model-indicated change in total atmospheric CO_2, however in order to directly compare our results with those of *Sprague et al.* [2007], we do not herein account for the change in total atmospheric amount of CO_2 and the influence this has upon the globally averaged noncondensable gas mixing ratio. If the enhancement values (both GRS-derived and -simulated) took account of the change in the total atmospheric mass through the course of the annual cycle, the south polar enhancement values would be reduced and the north polar values would be increased. It is reassuring to note that the relative enhancement of noncondensable gas in the model at 48°N latitude bin remains consistent with the VL2 GCMS values (within a couple of percent) for $L_s = 135°$ throughout the 4+ Martian year simulation.

[26] Temporally, the simulated south polar enhancement begins increasing (values noticeably greater than one) at $L_s = 30°$ (early southern autumn), monotonically increases to a peak value of three at $L_s = 120°$ (early southern winter), and subsequently monotonically declines to a value of one at $L_s = 180°$ (start of southern spring). Thereafter, during southern spring and summer, the south polar enhancement remains at or below a value of one. While the simulated temporal variation of the enhancement agrees well with GRS-derived results, including the lack of substantial high-frequency variability, the simulated enhancement peak is a factor of two smaller than the GRS-derived peak value.

[27] At high northern latitudes, the simulated enhancement value exceeds unity shortly after the start of northern autumn ($L_s = 180°$), increases to a temporally-broad peak value of ~1.5 extending from $L_s = 240°$ through $L_s = 350°$ (late northern autumn through late northern winter), and thereafter declines below a value of unity at $L_s = 15°$ (early northern spring). Enhancement values remain below unity (with a minimum of 0.7 at $L_s = 60°$) through late northern summer ($L_s = 165°$). The peak enhancement value of ~1.5 is a factor of two smaller than the GRS-derived peak value of three. It should be noted, however, that the GRS-derived enhancement values exhibit much greater "high-frequency" (several tens of degrees of L_s) variability than do the south polar results; the simulated north polar results do not exhibit such high-frequency enhancement variability. The model is unable to match the high-frequency GRS-derived oscillations in the north polar data. Only two GRS-derived northern winter enhancement values possess magnitudes that, in relation to their respective error bars, are well above a value of unity. A smoothing curve fit through the GRS-derived north polar enhancement values results in a maximum enhancement value less than two, in better agreement with the simulation's peak enhancement value of ~1.5.

[28] The GRS-derived polar enhancement, while being larger in magnitude than those simulated, are still smaller than the enhancement values that would be expected (factor of nine at high southern latitudes, 3.5-fold at high northern latitudes) if the noncondensing gases were retained in the atmospheric column above the seasonal caps (Figure 2). These differences are an indication that "mixing" with lower latitude air (CO_2 and noncondensable) is occurring at both caps. Our GCM results, including both the noncondensable gas abundances and the wind and pressure (atmospheric mass) fields, permit identification of those components of the circulation responsible for the net poleward transport of noncondensable gas during seasonal cap growth and decay.

[29] It has been documented that Martian topography and seasonal dust loading produce asymmetries in the eddy activity for a given season between the northern and southern hemisphere [*Barnes et al.*, 1993]. To determine the role that meridional (north-south) transport of noncondensable gas plays in the temporal and magnitude variations of the polar enhancement, we investigated the various simulated circulation components involved in the simulated polar enhancement. The fluxes arising from several components of circulation are determined using the formulation of *Peixoto and Oort* [1992]. The total noncondensable gas flux can be decomposed into three terms: mean meridional circulation, stationary eddies, and transient (or traveling) eddies.

[30] The total transport of noncondensable gas at a given latitude is denoted $[\overline{qv}]$, where q is the mass of noncondensable gas in kg/m^2, v is the meridional wind in m/s, [] is a zonal mean, and (overbar) is a temporal mean over 20 sols. The total transport can be represented by the sum of the mean meridional (or zonal mean) circulation, stationary eddies, and transient eddies according to *Peixoto and Oort* [1992]. The sum of these respective terms is as follows:

$$[\overline{qv}] = [\bar{q}][\bar{v}] + [\,\overline{q^*}\,\overline{v^*}\,] + [\,\overline{q'v'}\,] \quad (1)$$

with (*) representing deviation from the zonal mean and (') representing deviation from the temporal mean. For further discussion on this decomposition, see *Montmessin et al.* [2004]. This calculation is applied over sigma surfaces in the model and holds true so long as there are no large topographical variations. For this reason, this calculation is only applied to middle- and high-latitude regions where the topography is zonally symmetric. Figures for the decomposition will thus only represent results poleward of 45°.

[31] Understanding the difference in the characteristic enhancement between the south polar region and the north lies in the decomposition of the noncondensable transport. Figure 8 illustrates the decomposition of the total noncondensable gas flux in the model over one Martian year. The decomposition of the model results demonstrates that the zonal mean circulation (thermally direct circulation driven by the differential heating between the equatorial and polar regions), in conjunction with the condensation flow, is responsible for the transport of nondepleted air onto the pole during the fall and winter seasons, and stationary

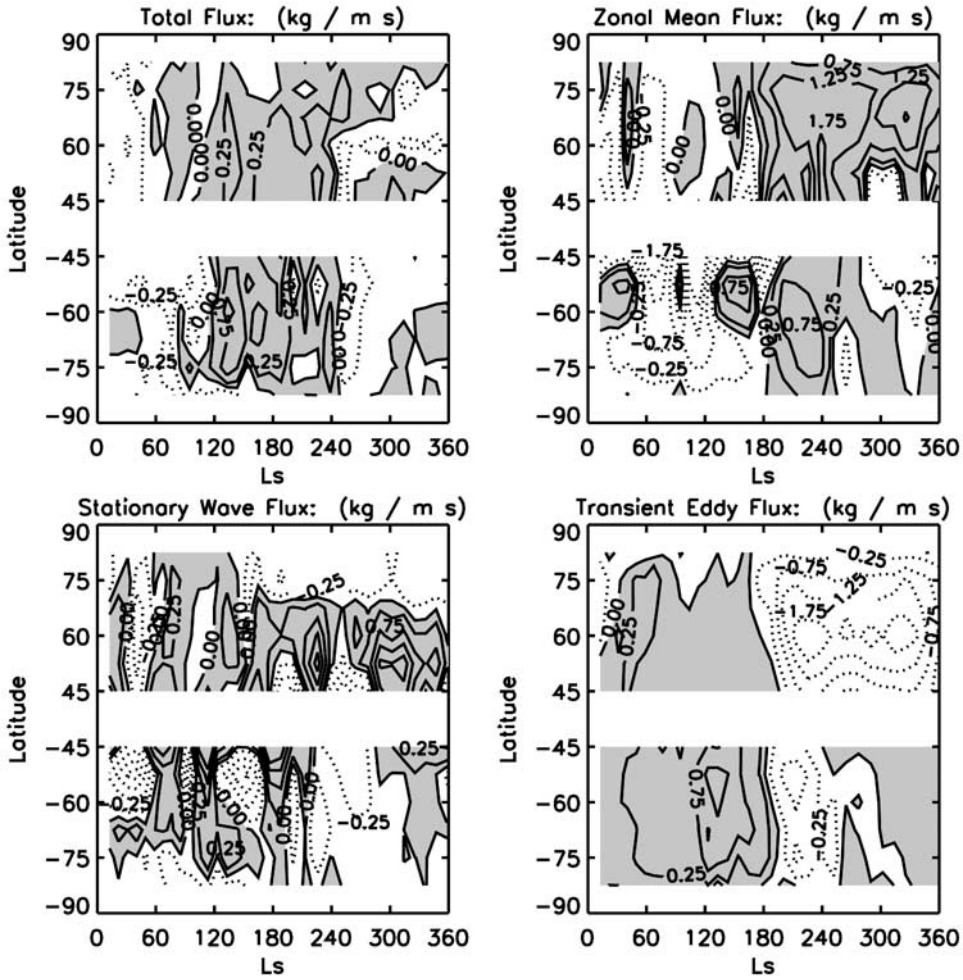

Figure 8. The vertically integrated meridional flux (kg m^{-1} s^{-1}) of noncondensable gas as a function of L_s and latitude generated in the nominal GCM simulation is shown. The total flux is a summation of the zonal mean flux, stationary wave flux, and the transient eddy flux, with these components defined according to the formulation by *Peixoto and Oort* [1992]. Values of the flux magnitudes equatorward of 45° are not shown because large topographic features in these regions result in improper partitioning of the flux due to the model sigma (normalized pressure) vertical coordinate employed. Contour levels are −1.75, −1.25, −0.75, −.25, 0, 0.25, 0.75, 1.25, and 1.75 kg m^{-1} s^{-1}. The shaded region represents all values greater than zero (northward flux).

waves and transient eddies are responsible for transport out of the polar regions during these seasons of enrichment. Figure 8 demonstrates that the transient eddies in the polar regions may be the key to the characteristic differences between the south and north polar enhancements. During southern fall and early winter, transient eddies are weak, much weaker than their northern brethren, and allow for the noncondensable gas abundance to increase monotonically. This hemispherical difference in transient eddy strength is consistent with previous analysis of TES data [*Barnes*, 2006; *Banfield et al.*, 2004] and prior numerical studies [*Barnes et al.*, 1993; *Basu et al.*, 2006]. At $L_s \sim 110°$, the southern hemisphere transient eddies strengthen, coinciding with the initiation of a decline in south polar noncondensable abundance. This increase in strength in the transient eddies is further underscored in Figure 9, where the noncondensable gas flux into the polar region (75° latitude) from the individual components of the general circulation are plotted as a function of L_s. Transient eddies grow to be twice as strong as stationary waves from $L_s \sim 110°$ to 180° (the period of time when the enhancement is being reduced). During this time the zonal mean circulation is still strong and transporting noncondensable gases and CO_2 into the south polar region. In fact, the polar cap continues to grow through this time, peaking at $L_s \sim 180°$, indicating that enhanced "air" is continuing to be produced even while the south polar enhancement values are declining.

[32] The north polar region does not get the opportunity for a large monotonic increase in noncondensable gases because the transient eddies are very strong from the outset of northern fall (Ls ~ 190°) and persist throughout the whole of northern winter. Figure 10 shows that the transient eddy flux into the north polar region (75°N) during almost the whole of northern fall and winter are a factor of two larger than the stationary eddies. These results support the findings of *Barnes* [2005], whose analysis of the MGS TES

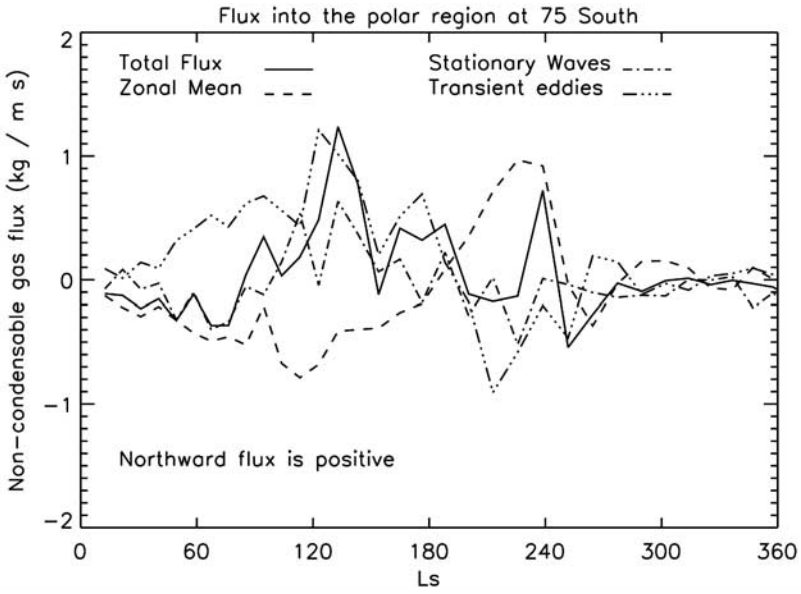

Figure 9. The noncondensable gas flux (kg m^{-1} s^{-1}) of the individual components of the general circulation into the south polar region (75°S) is plotted as a function of L_s. Starting at $L_s \sim 110°$, transient eddies grow to become twice as strong as stationary waves until $L_s \sim 180°$. During this time, the noncondensable gas enhancement is being reduced by atmospheric transport out of the polar region. Positive flux is northward.

atmospheric temperature data leads him to speculate that the difference in character between the polar enhancements can be explained by the difference in the transient eddy strengths over the opposing poles.

[33] Noncondensable gases in the polar regions on Mars increase in both absolute and relative abundance. Figures 6 and 7 illustrate the increase of noncondensable gases relative to VL2 measurements. However, referring back to Figure 5, this figure demonstrates that there is an increase in the absolute abundance (g/cm^2) of noncondensables as well. This increase is fivefold from min-to-max in the south and twofold from min-to-max in the north as the absolute abundance of noncondensable gases changes with season. The maximum value of absolute abundance in both the southern and northern hemispheres are similar (~1.5 g/cm^2), but the relative abundance between the hemispheres is separate by a factor of two. This occurs because of the factor of two difference in the annual mean surface pressure. If not for the strong, protracted transient eddies in the northern hemisphere, the absolute abundance of noncondensable gases in the north might double that in the south,

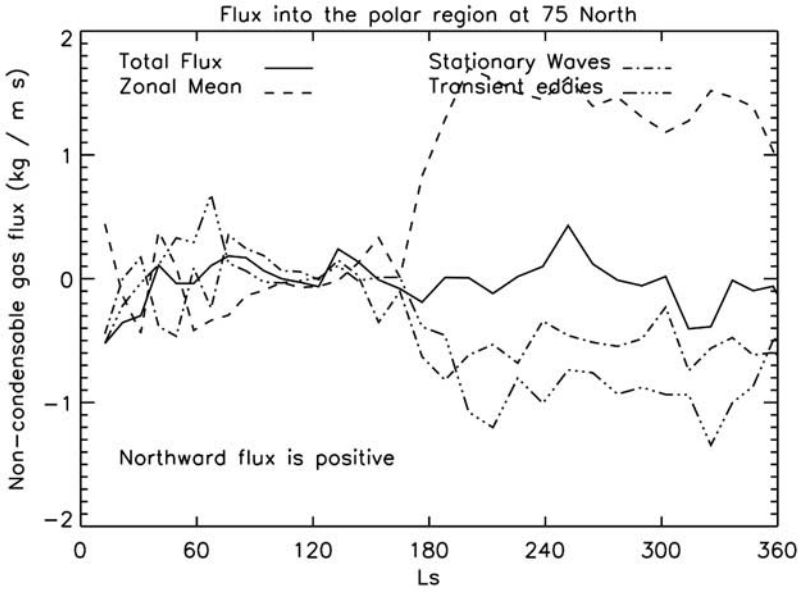

Figure 10. Same as Figure 9, but for the north polar region.

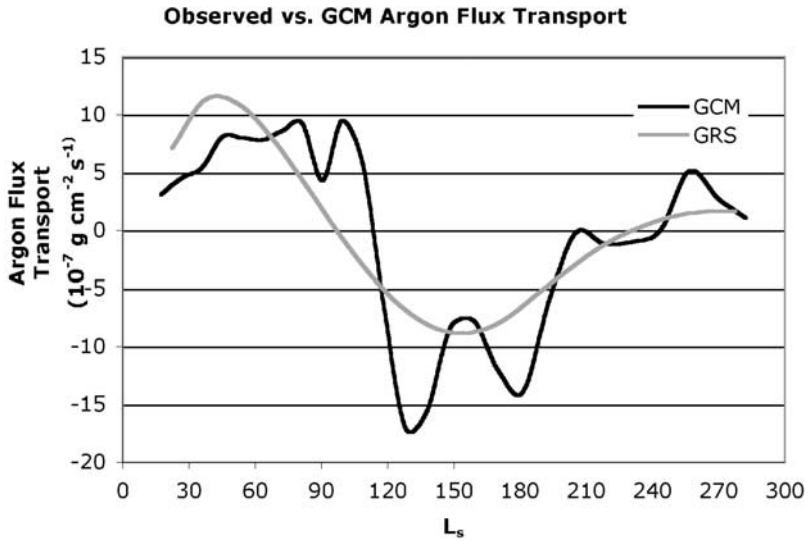

Figure 11. Mars Odyssey GRS-data-derived and GCM-simulated argon meridional flux magnitude into the south polar region (10^{-8} g cm^{-2} s^{-1}).

producing a relative abundance of equal magnitude over both winter poles.

[34] The annual mean atmospheric CO_2 column abundance over the south pole in the model is ~10.0 g/cm^2. Thus, with the global reservoir of noncondensable gas abundance at 4.7%, the average noncondensable gas column abundance can be assumed to be 0.47 g/cm^2. If the pole was isolated from the rest of the planet (i.e., mixing away from the pole did not occur until CO_2 condensation ceased), then the ~90.0 g/cm^2 of CO_2 ice condensed at the pole in the model would suggest a maximum abundance of 4.7 g/cm^2 noncondensable gas over the pole during winter (or 47% of the total atmospheric column). The absolute column abundance of noncondensable gases in the model reaches a maximum value of ~1.5 g/cm^2 at the south pole (Figure 5). The 4.7 g/cm^2 of noncondensable gas is an upper limit on the absolute abundance, and the difference between the upper limit and the model maximum indicates the strength of eddy mixing off the pole in the model. Also, since the *Sprague et al.* [2007] data produce a south polar enhancement that is a factor of two greater than the model, we can infer that the absolute south polar noncondensable gas column abundance on Mars is also a factor of two greater than the model. Thus the actual noncondensable gas column abundance on Mars can have an inferred value of ~3.0 g/cm^2, or 30% of the atmospheric column. Such a high ratio of noncondensable gases in an atmospheric column brings back to the foreground the discussion of the importance of the noncondensable gas enhancement to the temperature depression seen by the Viking Orbiters. Not to go without mentioning, the difference between the inferred value (3.0 g/cm^2) and the maximum column abundance for noncondensable gas in the model (1.5 g/cm^2) suggests that mixing off the south pole in the GCM is too strong by a factor of two.

[35] To obtain a better understanding of how well the model is capturing the atmospheric dynamics, we compare the flux transport and estimated meridional mixing coefficient in the model to those values calculated by *Sprague et al.* [2004] using the GRS-derived south polar argon abundances. *Sprague et al.* [2004] estimate the meridional mixing coefficient (K_x) from

$$K_x = \left(\frac{\Delta x}{\Delta f_{Ar}}\right)\left[v_x f_{Ar} - \left(\frac{F_{Ar}}{\rho}\right)\right] \quad (2)$$

where Δx is the distance necessary for argon to be transported away from the south polar region, 30° of latitude in arc length, Δf_{Ar} is the difference in argon mixing ratio between the south polar region (75°S to 90°S) and the seasonally adjusted VL2 measurements, v_x is the north-south wind speed [CO_2 mass transport/(VL2 mean density * area of imaginary cylinder surrounding the polar region)], f_{Ar} is the argon mixing ratio at the VL2 site for the appropriate L_s, ρ is the ambient atmospheric mass density at 45°S (30° latitude away from the polar region), and F_{Ar} is the argon flux transport (g cm^{-2} s^{-1}). The argon flux transport is calculated by taking the time rate of change of argon mass in the south polar region as it passes through an imaginary cylinder encompassing the 75°S latitude circle. Cylinder height changes with season because of the change in atmospheric scale height. The formulation of F_{Ar} appears in *Sprague et al.* [2004] to explore the net flux of Ar using measurements of the GRS. Lacking local wind measurements, this formulation is necessarily conceptually different from that described by *Peixoto and Oort* [1992], and thus contains dissimilar units. For further discussion on this formulation, see *Sprague et al.* [2004].

[36] Figure 11 compares the simulated argon flux transport (F_{Ar}) into the south polar region with that derived from the GRS data, positive flux is poleward. Argon flux onto the pole in the model is similar to that derived from the GRS data. While the simulated flux is slightly weaker in magnitude than the GRS-derived flux, it is seasonally more extensive. Even though the simulated south polar enhancement is half that derived from the GRS data, the similarity in magnitude between the argon fluxes into the south polar region is consistent with the model reproducing an appro-

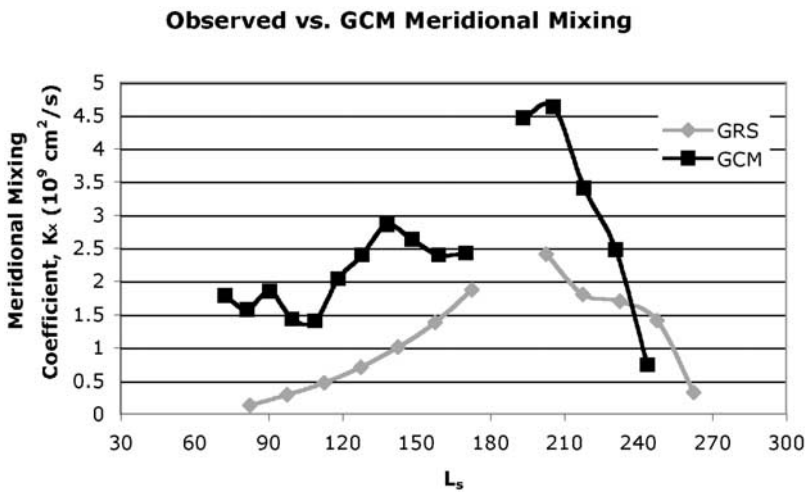

Figure 12. GRS-data-derived and GCM-simulation-derived meridional mixing coefficients (10^9 cm^2 s^{-1}) of noncondensing gas consistent with the observed and simulated time and latitude enhancement variations.

priate CO_2 cycle. It is expected that the simulated condensation flow onto the south polar cap, which is responsible for transporting nondepleted air from lower latitudes into the polar region, is similar in magnitude to observation. Figure 12 illustrates that the reason for the model underpredicting the argon enhancement in the south polar region is not for lack of transport into the region, but rather that eddy mixing (cm^2 s^{-1}) out of the polar region is too strong by a factor of two in the model.

[37] The lack of a pole point and the convergence of meridians require the use of numerical filters in the polar regions to reduce computational instability. We have adjusted the filter length by a factor of three in both directions from the nominally used value in the previous simulation to study how the filter length affects the development of the noncondensable gas enhancement. Reducing the filter length shows no significant change in the enhancement magnitudes, nor in the general circulation components. By increasing the filter length, the absolute and relative abundances of the noncondensable gas in the polar regions are reduced by ~30% when compared to the current Mars simulation above, to a maximum south polar enhancement of twofold. This is still a significant result since the noncondensable gas in the Martian atmosphere would only be enhanced by 1.3-fold, or 30% increase, due to the change in the global mean pressure from CO_2 condensation. The general circulation components are qualitatively similar to the current Mars simulation, but show a near uniform decrease in strength of ~30%. While the results of the noncondensable gas enhancement due to the changing of the polar filter lengths deserve further study, we find that these results do not impair our final conclusions.

[38] In order to examine the effects spatial resolution within the model has on the predicted enhancement values, the model is run with a horizontal resolution of 4.0° × 5.0° (latitude versus longitude). The model enhancements for both the high-resolution (4.0° × 5.0°) and low-resolution (7.5° × 9.0°) simulations are nearly identical. The general circulation components are also both qualitatively and quantitatively consistent between the two simulations. With resolution not being an issue when considering the global-scale factors that determine the polar enhancement characteristics, all other simulations are run at low resolution for reasons concerning both time and storage space.

[39] Having addressed the dynamical processes (components of transport, CO_2 condensation, etc.) that affect the observed noncondensable gas enhancement, this paper turns toward studying the effect that Mars specific physical parameters (surface properties, orbital characteristics, atmospheric dust load, etc.) have on the dynamic processes. These physical parameters are isolated to the fullest extent reasonable and the effects they have on the dynamical processes responsible for enhancement are studied. Studying the effects topography, eccentricity and opacity have on the noncondensable gas enhancement produces a fuller understanding of the enhancement phenomenon and creates the picture of how noncondensable gas enhancements were affected by prior Martian epochs.

6.2. Topographic Relief

[40] Continental-scale orography on Mars greatly influences global atmospheric circulation patterns. Martian topography produces asymmetries in the eddy activity for a given season [*Barnes et al.*, 1993] and these eddies are produced and decay preferentially within geographically (latitudinally and longitudinally) confined regions [*Hollingsworth et al.*, 1996]. This topographical influence on the atmospheric eddies of Mars plays an important role in the transport of heat, momentum and noncondensable gas onto the poles [*Hollingsworth et al.*, 1996]. By eliminating topographic variation in the GCM, we remove much of the primary driving mechanism for stationary eddies, and also affect the traveling eddy amplitudes and seasonality. This allows us to study the direct effects current Martian topography has on the noncondensable gas enhancement.

[41] Martian topography is set to be of uniform altitude (equal to the Martian datum) everywhere to remove the effects it has on the components of transport. All other initial conditions are the same as current Mars. The enhancement factor of noncondensable gas increases in

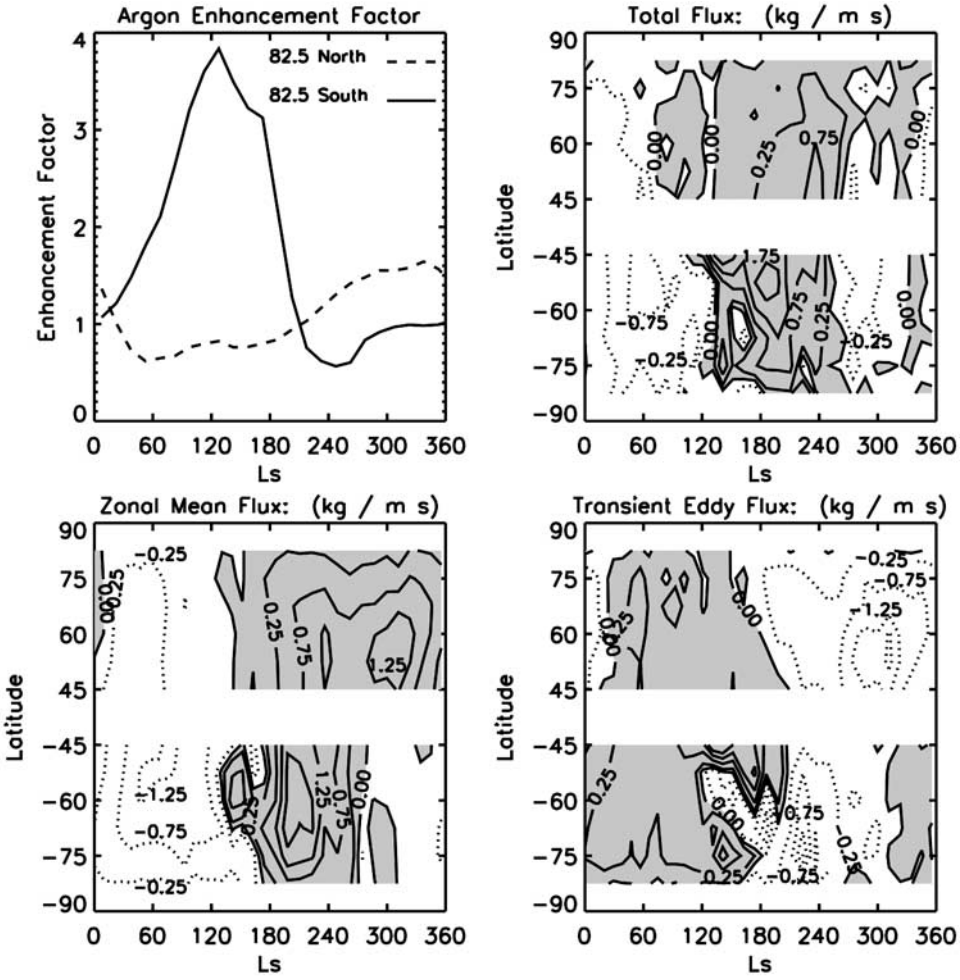

Figure 13. Simulated noncondensable gas column integrated enhancement factor (top left) and meridional flux magnitudes, like those in Figure 8, but here for a GCM simulation where topographic variations have been eliminated, minimizing the influence of stationary waves (whose results are not shown). Note that both the north and south polar noncondensable gas enhancement magnitudes are increased compared to the results obtained with topography included (Figure 8).

both hemispheres (Figure 13). This occurs because of the effect that topography has on stationary and transient eddies (the components of the circulation responsible for transport off the polar regions during fall and winter). First, with a uniformly smooth surface, topographically induced stationary eddies do not develop. Second, transient eddies weaken over both polar regions without the presence of Martian topography. The increase in the enhancement over the north polar region is less than that in the south because in addition to the transient eddies weakening, the zonal mean flux onto the winter cap in the north is substantially reduced.

6.3. Eccentricity

[42] Martian eccentricity produces asymmetry in the severity of winter during the polar night. Mars' highly eccentric orbit ($\varepsilon \sim 0.1$) currently produces a longer, colder winter at aphelion for the winter pole (currently the southern hemisphere). The current eccentricity is a factor in the increased atmospheric CO_2 condensation over the south pole during winter, contributing to the current dichotomy in the winter noncondensable gas enhancement between the two winter poles. Through the removal of Mars' eccentric orbit in the GCM (via circularizing the orbit), we are able to discern the effects the current eccentricity has on Mars' noncondensable gas enhancement and the polar asymmetry of this enhancement. These effects are influenced by the dichotomy in the winter polar CO_2 condensation and by hemispherical differences in the atmospheric circulation due to the aphelion winter hemisphere receiving 40% less sunlight than its perihelion winter counterpart.

[43] With all other initial conditions the same as current Mars, Mars' eccentricity is set to zero in the model. As expected, the asymmetry in the magnitude of the enhancement factor decreases. Under current conditions, the enhancement of noncondensable gas is a factor of two greater in the south. When eccentricity is set to zero, the south pole enhancement factor decreases by 17% from current Mars conditions (Figure 14), while the north pole enhancement increases by 15%. The change in the enhancement in the north coincides with a similar increase in CO_2 ice condensation over the cap (Figure 15). In the south, there is only an 11% decrease in CO_2 ice over the cap,

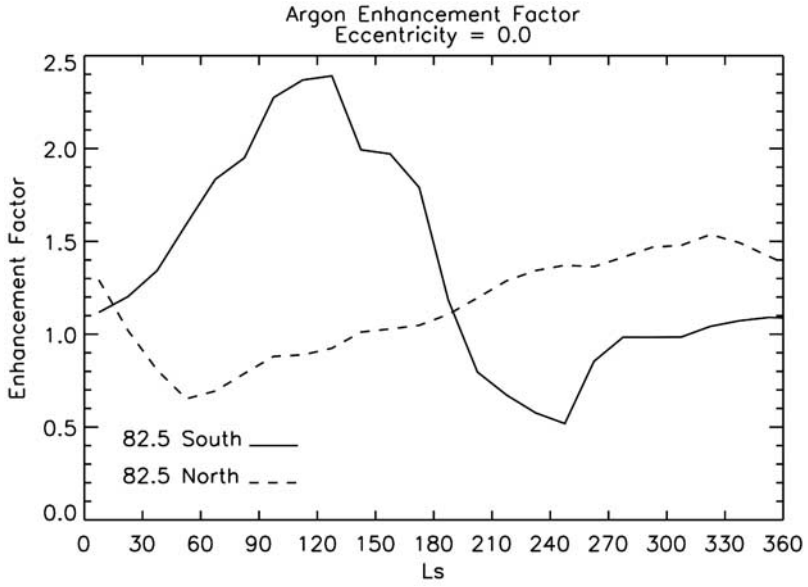

Figure 14. Simulated north and south polar noncondensable gas column integrated enhancement factor, like that shown in Figures 6 and 7, but here for a GCM simulation in which Mars' orbital eccentricity has been set to zero (its nominal value is 0.087).

indicating that the rest of the change in the enhancement is due to a change in the strength of polar mixing. In effect, by setting Mars' highly eccentric orbit to zero, northern winter becomes longer and southern winter shorter than under current conditions. More CO_2 condensing out in the north polar region leaves more noncondensable gas behind, producing a greater enhancement, while less CO_2 condensing out over the south produces the opposite effect.

6.4. Billiard Ball

[44] To ensure that all results concerning the dichotomy in the polar noncondensable gas enhancement are due to physical processes ascribed to Mars (i.e., topography, orbital characteristics, etc.) and not to errors induced by the solution of the dynamical equations, we produce a simulation using a "billiard ball" planet, hereafter, BB. The BB simulation parameters contain spatially uniform flat topography, minimal atmospheric dust load, thermal inertia of 300, surface albedo of 0.23, and orbital eccentricity of zero (while retaining a 25° obliquity). The seasonal cap emissivity and albedo are set to be uniform in the northern and southern hemispheres (the values for the southern cap are used in both hemispheres). The model produces hemispherically symmetric enhancement over the poles as well as symmetric zonal mean fluxes and transient eddies (Figure 16). Both poles obtain a factor of two enhancement by early winter, suggesting that the polar noncondensable gas enhancement

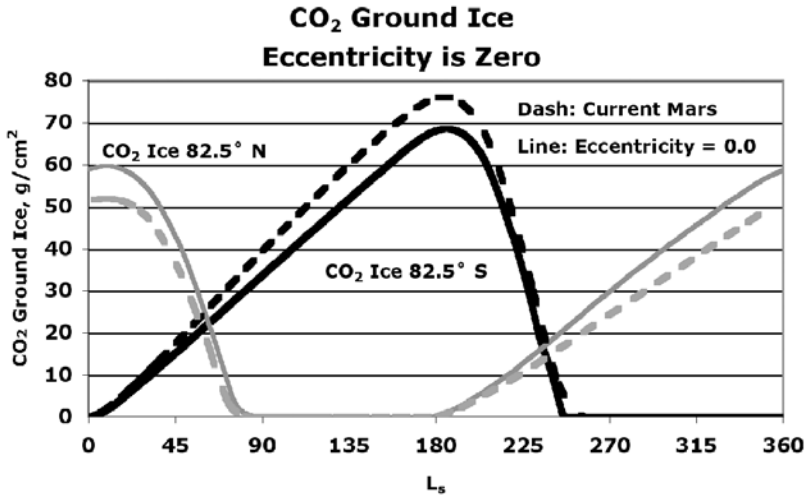

Figure 15. Simulated CO_2 ground ice column abundance (g/cm^2) at high northern and southern latitudes generated in the nominal GCM simulation (dashed curves) and in the GCM simulation with an orbital eccentricity of 0.0 (solid curves).

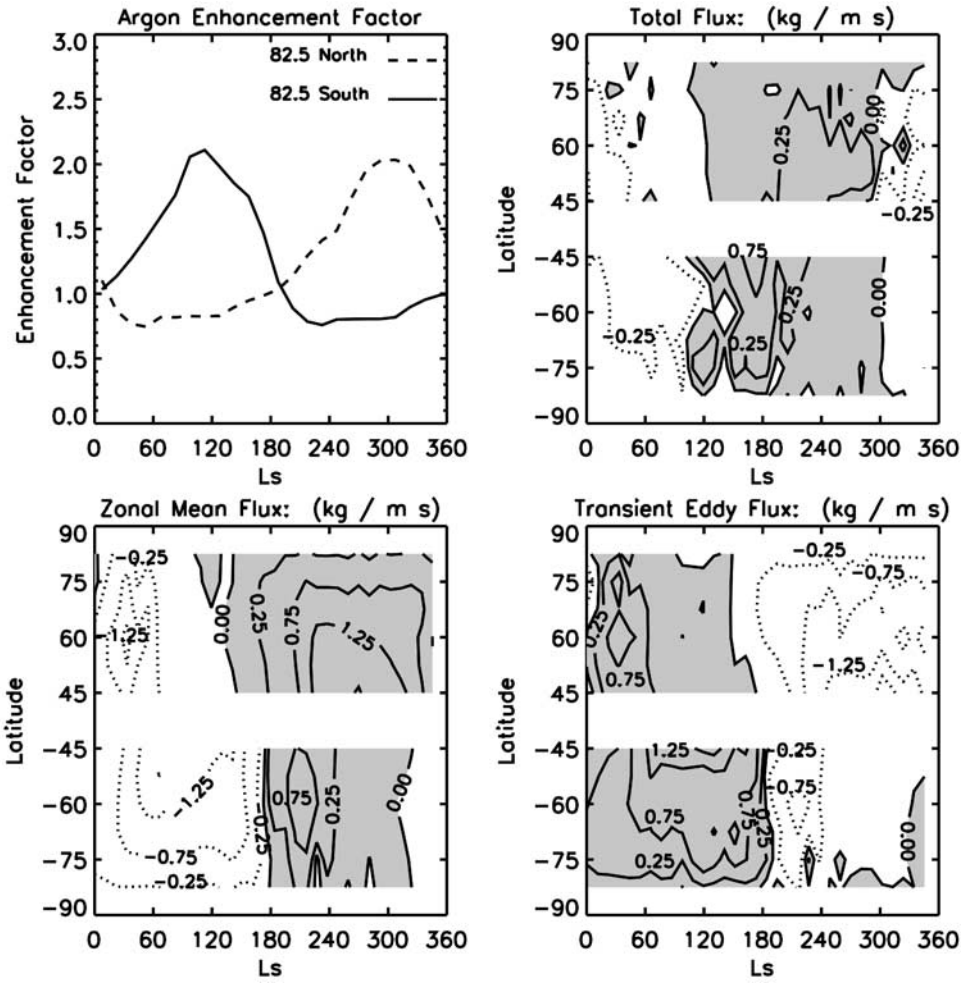

Figure 16. Simulated noncondensable gas column integrated enhancement factor (top left) and meridional flux magnitudes, like those in Figure 13, but here for a BB minimal atmospheric dust GCM simulation for which all surface variations (topography, albedo, thermal inertia, seasonal cap properties) have been eliminated and orbit eccentricity has been set to zero. Both the north and south polar noncondensable gas enhancement magnitudes achieve the same maximum values and are smaller than the south polar maxima indicated in Figures 6 and 13.

dichotomy in the model is due to the physical processes and not to errors in the solution of the dynamical equations.

6.5. Opacity and Cap Emissivity

[45] In the final simulations, BB models are run with one of each of two possible factors that might induce a dichotomy in magnitude of the polar enhancement: (1) dust opacity and (2) hemispherically asymmetric cap emissivity and albedo. Running two BB simulations, one with 0.4 uniform dust opacity and another with 1.0, does not change the polar symmetry of the enhancement magnitude seen in the BB model when run with minimal opacity. Opacity does, however, affect the dynamic range of the enhancement. Increasing the opacity in the BB model to a globally uniform value 0.4 increases both the minimum and the maximum noncondensable gas abundance (Figure 17). The initial increase in opacity delays the onset of the transient eddies to mid-winter, allowing for greater enhancement over the poles. When the transient eddies do finally arrive, they are stronger than at lower opacities, driving out more of the enriched atmosphere and creating a deeper depletion. This increase is purely a circulation effect, as the difference in CO_2 deposition between the two models is negligible (a few percent) (Figure 18).

[46] As the global mean opacity nears $\sim$1.0, the transient eddy flux becomes dominant earlier in the winter season. This dominance manifests itself with the transient eddies becoming stronger in magnitude and penetrating more deeply into the winter polar region (Figure 19). Transient eddies become the dominant mode of transport over the zonal mean flux earlier in the season as opacity increases near optical depth of unity. Thus enhancement over the pole begins to decline with increasing opacity near optical depth of unity. As mentioned before, without any topographic relief, the effects of stationary eddies are trivial.

7. Discussion

7.1. Summary

[47] The NASA Ames GCM, under current Martian conditions, produces a winter season polar noncondens-

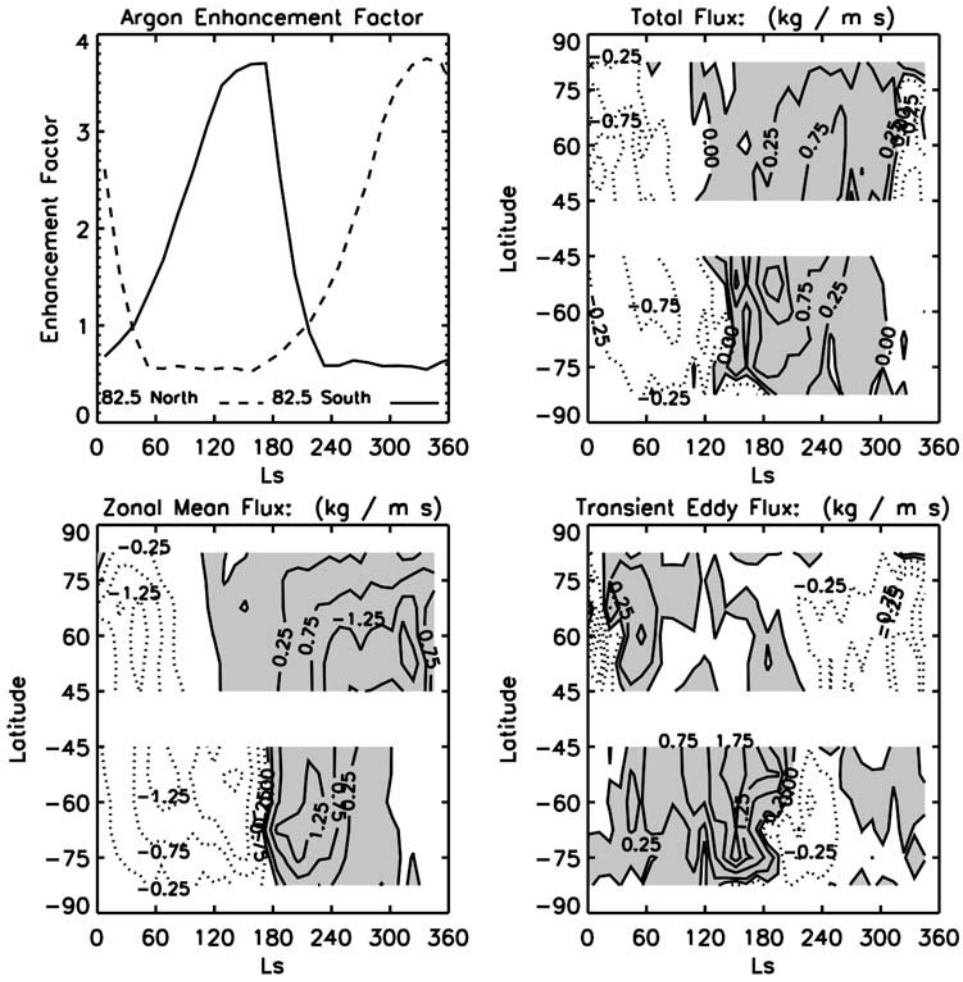

Figure 17. GCM-simulated noncondensable gas column integrated enhancement factor (top left) and meridional flux magnitudes, like those in Figure 16, but here for a "billiard ball" zero-eccentricity GCM simulation driven with a globally uniform dust optical depth of 0.4 (at the 6.1 mbar level).

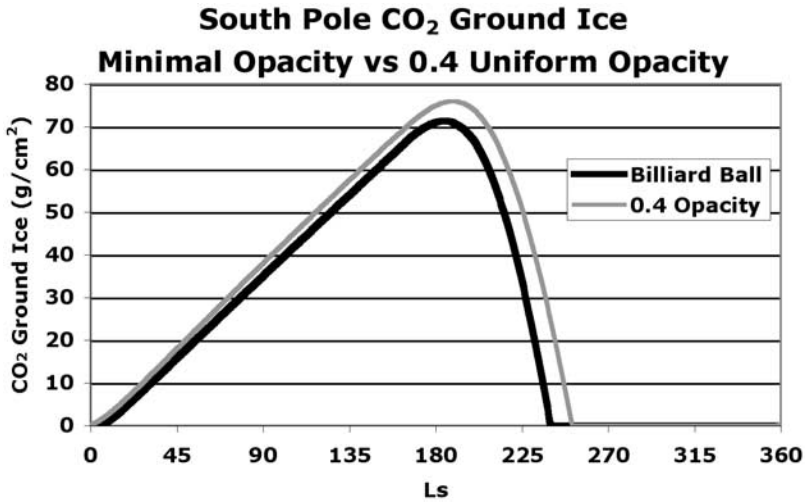

Figure 18. GCM-simulated CO_2 ground ice column abundance (g/cm^2) at 82.5°S latitude from a "billiard ball" simulation with minimal atmospheric dust abundance (corresponding to the results in Figure 16) and with an atmospheric dust optical depth of 0.4 (corresponding to the results of Figure 17).

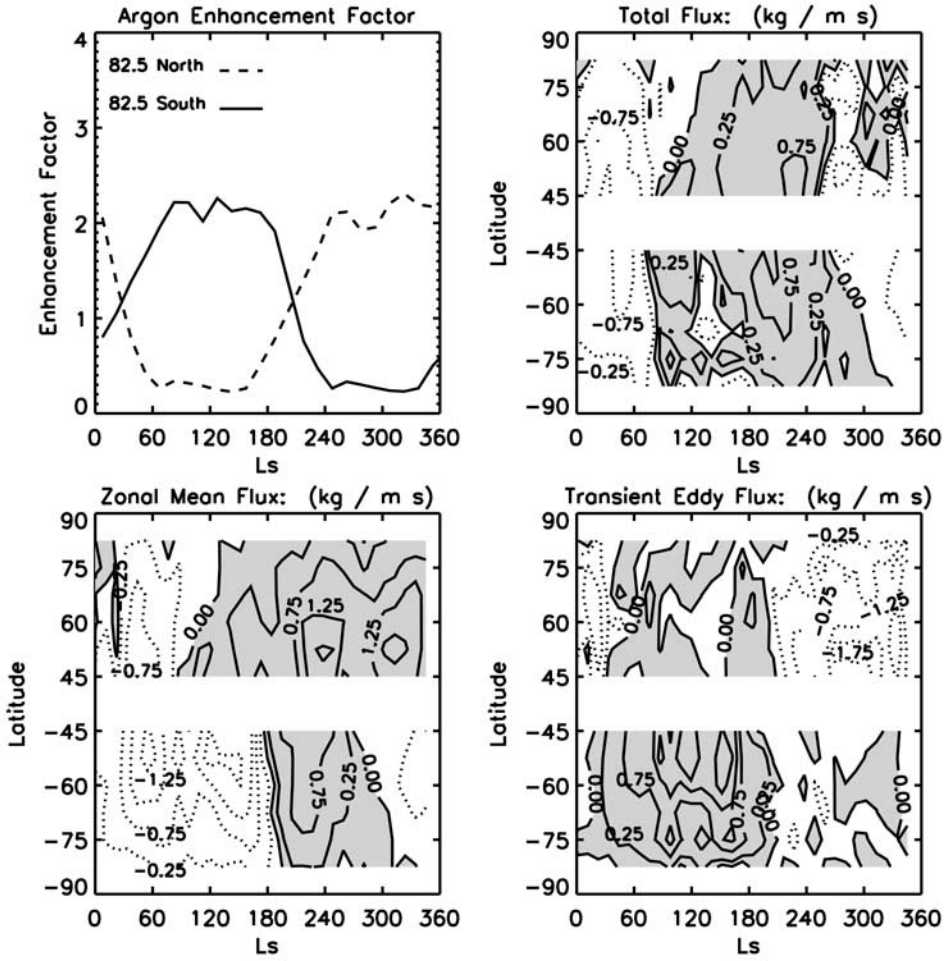

Figure 19. Like the results shown in Figure 17, but here for a "billiard ball" zero-eccentricity GCM simulation driven by a dust optical depth of 1.0.

able gas enhancement that is hemispherically asymmetric. Temporal and magnitude asymmetries arise within the model. This asymmetry qualitatively fits the observed data derived from GRS [*Sprague et al.*, 2007]. The threefold enhancement in the south polar region and the 1.4-fold enhancement in the north is up to a factor of two less than the GRS-derived enhancements but are temporally consistent with observations. The model lacks large fluctuations in the north polar simulated enhancement and we still do not understand the small-scale circulation source of these oscillations. In the southern hemisphere, the difference between the GRS-derived enhancement factor and the model-derived enhancement factor indicates that eddy mixing off the south pole in the GCM is too strong by a factor of two. Monotonic growth of the enhancement in the southern hemisphere is due to the nature of the transient eddies in the southern hemisphere. Since the transient eddies are weaker than their counterparts in the north and do not become strong until late winter, their lack of presence may be the principal cause for the large enhancement over the south polar region. Without the presence of transient eddies, the south polar noncondensable gas abundance would reach an astonishing 47% of the total atmospheric column mass.

7.2. Enhancement Underprediction by the Ames GCM

[48] In the Ames GCM, vertical layers are defined according to a sigma pressure coordinate system, $\sigma = p/p_o$. When CO_2 condensation and sublimation occur, the change in surface pressure (p_o) artificially moves the σ layers. During condensation, this movement can induce an enhancement of noncondensable gases in all vertical layers rather than just in the layer that condensation is occurring. *Forget et al.* [1998] provide a numerical solution for this problem but which is not included in our simulations presented in this paper. The *Forget et al.* [1998] "correction" is meant to fix the artificial movement of σ layers by enriching the condensing layers at the expense of the other layers in a column. In effect, the greatest condensation is occurring near the surface, creating a decreasing abundance of noncondensable gas with increasing altitude.

[49] The simulations in this paper produce a local maximum of noncondensable gas abundance in the polar column at ~0.5 mbar level. Upon applying the *Forget et al.* [1998] correction to the Ames GCM, this problem was still found to exist. Further inspection found that in the Ames GCM, as expected, CO_2 condensation is largest near the surface. However, large CO_2 condensation occurs in the vertical layers corresponding to the pressure levels between 0.1 and 0.8 mbars as well. This creates a local maximum of

noncondensable gas enhancement in the model at these altitudes. Because of the large quantities of mid-level CO_2 condensation, the *Forget et al.* [1998] correction only serves to augment the noncondensable gas enhancement at this altitude, not reduce it.

[50] The inability of the Ames GCM to produce a decreasing abundance of noncondensable gas as a function of height, instead producing a local maximum at the 0.5 mbar level, may contribute to the model's inability to produce an enhancement equivalent to observation. The higher altitude at which this enhancement is occurring may put the noncondensable gas at an altitude of greater equatorward mixing. The excess equatorward mixing caused by the local maximum of noncondensable gas at 0.5 mbars would also contribute to the model's apparent overly strong eddy mixing off the pole when compared to *Sprague et al.* [2004]. Thus the difference between the eddy mixing in the model and in the *Sprague et al.* [2004] results would not be a function of the strength in the eddy mixing, but rather a function of the height at which the noncondensable gas was placed. If all the CO_2 condensation in the model were occurring near the surface, it may be possible to reconcile the factor of two difference between the model results and the observations.

7.3. Prior Martian Epochs

[51] During an earlier era in Martian history, the enrichment of noncondensable gases over the winter poles would have changed as a function of the changing physical characteristics of the red planet (eccentricity, obliquity, opacity, etc.). As Martian eccentricity cycles between 0 and 0.12 every 2.5 Myr [*Laskar et al.*, 2004], so will the difference in the peak magnitude of noncondensable gases between the two poles vary. In times of lesser eccentricity, the difference in peak magnitude of noncondensable gases between the two poles will decrease. As the orbit becomes less eccentric, the perihelion distance moves further away from the sun and/or the aphelion distance between Mars and the sun moves closer than is currently positioned, thus altering the amount of CO_2 to be condensed over the poles during these periods. The end effect in reducing the eccentricity is to reduce the difference in the total CO_2 condensed over each pole during fall and winter. In times of greater eccentricity, the difference in peak magnitude between the two poles will increase as the opposite effect holds true. Circularizing the Martian orbit does not completely remove the difference in peak magnitude between the north and south pole. The strength and season, when transient eddies occur, play a primary role in determining this difference, and this is determined by a number of factors, including topographic relief and atmospheric dust opacity.

[52] At times of higher obliquity, GCM simulations suggest Mars becomes a dustier environment [*Haberle et al.*, 2003; *Newman et al.*, 2005; *Kahre et al.*, 2006]. As the global mean atmospheric dust opacity increases, the dynamic range of the polar noncondensable gas enhancement increases. Up to dust opacities of 0.4, transient eddies weaken, allowing for greater enhancement over the poles. As the dust opacity approaches unity, transient eddies strengthen in magnitude beyond that under current Martian conditions and manifest themselves earlier in season and penetrate deeper into the polar region. This works against the noncondensable gas enhancement, reducing the enhancement compared to values at lower opacity.

[53] **Acknowledgments.** We wish to thank Bill Feldman for the GRS-derived thickness values of the northern CO_2 frost cap on Mars. Furthermore, a special thank you goes to Franck Montmessin and Jeff Hollingsworth for their advice on the calculation of the circulation decomposition. We are grateful to John Wilson and Scot Rafkin for their help and suggestions. Support for this work was provided by NASA Planetary Atmospheres Programs (NAG5-12123) and New Mexico Space Grant, and partial funding was provided by the Mars Data Analysis Program NNG04GJ94G and NSF/AFOSR ASTR award 103890/AST-0335665.

References

Banfield, D., B. J. Conrath, M. D. Smith, P. R. Christensen, and R. J. Wilson (2003), Forced waves in the Martian atmosphere from MGS TES nadir data, *Icarus*, *161*, 319–345.

Banfield, D., B. J. Conrath, P. J. Gierasch, R. J. Wilson, and M. D. Smith (2004), Traveling waves in the Martian atmosphere from MGS TES nadir data, *Icarus*, *170*, 365–403.

Barnes, J. R. (2003), Mars weather systems and maps: FFSM analysis of MGS TES temperature data, in *Sixth International Conference on Mars*, Abstract 3127, Lunar and Planet. Inst., Houston, Tex.

Barnes, J. R. (2005), Planetary eddies in the MGS TES data and winter argon transports, *Lunar Planet. Sci.*, *XXXVI*, Abstract 1267.

Barnes, J. R. (2006), FFSM studies of transient eddies in the MGS TES temperature data (abstract), paper presented at Second Workshop on Mars Atmosphere Modelling and Observation, Cent. Natl. d'Etudes Spatiales, Granada, Spain, 27 Feb. to 3 March. (Available at http://www-mars.lmd.jussieu.fr/granada2006/)

Barnes, J. R., J. B. Pollack, R. M. Haberle, C. B. Leovy, R. W. Zurek, H. Lee, and J. Schaeffer (1993), Mars atmospheric dynamics as simulated by the NASA Ames General Circulation Model: 2. Transient baroclinic eddies, *J. Geophys. Res.*, *98*(E2), 3125–3148.

Barnes, J. R., R. M. Haberle, J. B. Pollack, H. Lee, and J. Schaeffer (1996), Mars atmospheric dynamics as simulated by the NASA Ames General Circulation Model: 3. Winter quasi-stationary eddies, *J. Geophys. Res.*, *101*, 12,753–12,776.

Basu, S., J. Wilson, M. Richardson, and A. Ingersoll (2006), Simulation of spontaneous and variable global dust storms with the GFDL Mars GCM, *J. Geophys. Res.*, *111*, E09004, doi:10.1029/2005JE002660.

Boynton, W. V., et al. (2004), The Mars Odyssey Gamma-Ray Spectrometer Instrument suite, *Space Sci. Rev.*, *110*, 37–83.

Clancy, R. T., M. J. Wolff, and P. R. Christensen (2003), Mars aerosol studies with the MGS TES emission phase function observations: Optical depths, particle sizes, and ice cloud types versus latitude and solar longitude, *J. Geophys. Res.*, *108*(E9), 5098, doi:10.1029/2003JE002058.

Conrath, B. J. (1975), mal structure of the Martian atmosphere during the dissipation of the dust storms of 1971, *Icarus*, *24*, 36–46.

Ditteon, R., and H. Kieffer (1979), Optical properties of CO_2: Application to Mars, *J. Geophys. Res.*, *84*, 8294–8300.

Feldman, W. C., et al. (2003), CO_2 frost cap thickness on Mars during northern winter and spring, *J. Geophys. Res.*, *108*(E9), 5103, doi:10.1029/2003JE002101.

Feldman, W. C., et al. (2005), Topographic control of hydrogen deposits at low latitudes to midlatitudes of Mars, *J. Geophys. Res.*, *110*, E11009, doi:10.1029/2005JE002452.

Forget, F. (2004), Alien weather at the poles of Mars, *Science*, *306*, 1298–1299.

Forget, F., F. Hourdin, and O. Talagrand (1998), CO_2 snowfall on Mars: Simulation with a general circulation model, *Icarus*, *131*, 302–316.

Haberle, R. M., C. B. Leovy, and J. B. Pollack (1982), Some effects of global dust storms on the atmospheric circulation of Mars, *Icarus*, *50*, 322–367.

Haberle, R. M., J. B. Pollack, J. R. Barnes, R. W. Zurek, C. B. Leovy, J. R. Murphy, H. Lee, and J. Schaeffer (1993), Mars atmospheric dynamics as simulated by the NASA Ames general circulation model: 1. The zonal-mean circulation, *J. Geophys. Res.*, *98*(E2), 3093–3123.

Haberle, R. M., M. M. Joshi, J. R. Murphy, J. R. Barnes, J. T. Schofield, G. Wilson, M. Lopez-Valverde, J. L. Hollingsworth, A. F. C. Bridger, and J. Schaeffer (1999), General circulation model simulations of the Mars Pathfinder atmospheric structure investigation/meteorology data, *J. Geophys. Res.*, *104*(E4), 8957–8974.

Haberle, R. M., J. R. Murphy, and J. Schaeffer (2003), Orbital change experiments with a Mars general circulation model, *Icarus*, *161*, 66–89.

Hanel, R., et al. (1972), Investigation of the Martian environment by infrared spectroscopy on Mariner 9, *Icarus*, *17*, 423–442.

Hollingsworth, J. L., and J. R. Barnes (1996), Forced stationary planetary waves in Mars' winter atmosphere, *J. Atmos. Sci.*, *53*, 428–448.

Hollingsworth, J. L., R. M. Haberle, J. R. Barnes, A. F. C. Bridger, J. B. Pollack, H. Lee, and J. Schaeffer (1996), Orographic control of storm zones on Mars, *Nature*, *380*, 413–416.

James, P., H. Kieffer, and D. Paige (1992), The seasonal cycle of carbon dioxide on Mars, in *Mars*, edited by H. H. Kieffer et al., pp. 934–968, Univ. of Ariz. Press, Tucson.

Kahre, M. A., J. R. Murphy, and R. M. Haberle (2006), Modeling the Martian dust cycle and surface dust reservoirs with the NASA Ames general circulation model, *J. Geophys. Res.*, *111*, E06008, doi:10.1029/2005JE002588.

Kieffer, H. H., S. C. Chase Jr., E. D. Miner, F. D. Palluconi, G. Munch, G. Neugebauer, and T. Martin (1976), Infrared thermal mapping of the Martian surface and atmosphere: First results, *Science*, *193*, 780–786.

Kieffer, H. H., T. Z. Martin, A. R. Peterfreund, B. M. Jakosky, E. D. Miner, and F. D. Miner (1977), Thermal and albedo mapping of Mars during the Viking primary mission, *J. Geophys. Res.*, *82*, 4249–4291.

Laskar, J., A. C. M. Correia, M. Gastineau, F. Joutel, B. Levrard, and P. Robutel (2004), Long term evolution and chaotic diffusion of the insolation quantities of Mars, *Icarus*, *170*, 343–364.

Leovy, C., and Y. Mintz (1969), Numerical simulation of the atmospheric circulation and climate of Mars, *J. Atmos. Sci.*, *26*, 1167–1190.

Martin, T. Z. (1986), Thermal infrared opacity of the Mars atmosphere, *Icarus*, *66*, 2–21.

Montmessin, F., F. Forget, P. Rannou, M. Cabane, and R. M. Haberle (2004), Origin and role of water ice clouds in the Martian water cycle as inferred from a general circulation model, *J. Geophys. Res.*, *109*, E10004, doi:10.1029/2004JE002284.

Murphy, J. R., J. B. Pollack, R. M. Haberle, C. B. Leovy, O. B. Toon, and J. Schaeffer (1995), Three dimensional numerical simulations of Martian global dust storms, *J. Geophys. Res.*, *100*(E12), 26,357–26,376.

Neugebauer, G., G. Munch, H. Kieffer, S. C. Chase Jr., and E. Miner (1971), Mariner 1969 infrared radiometer results: Temperatures and thermal properties of the Martian surface, *Astron. J.*, *76*, 719–728.

Newman, C. E., S. R. Lewis, and P. L. Read (2005), The atmospheric circulation and dust activity in different orbital epochs on Mars, *Icarus*, *174*, 135–160.

Owen, T., K. Biemann, J. E. Biller, A. L. Lafleur, D. R. Rushneck, and D. W. Howarth (1977), The composition of the atmosphere at the surface of Mars, *J. Geophys. Res.*, *82*, 4635–4639.

Peixoto, J. P., and A. H. Oort (1992), *Physics of Climate*, Am. Inst. of Phys., New York.

Pollack, J. B., R. M. Haberle, J. Schaeffer, and H. Lee (1990), Simulations of the general circulation of the Martian atmosphere: 1. Polar processes, *J. Geophys. Res.*, *95*(B2), 1447–1473.

Prettyman, T. H., et al. (2004), Composition and structure of the Martian surface at high southern latitudes from neutron spectroscopy, *J. Geophys. Res.*, *109*, E05001, doi:10.1029/2003JE002139.

Smith, D. E., et al. (1999), The global topography of Mars and implications for surface evolution, *Science*, *284*, 1495–1503.

Smith, M. D. (2004), Interannual variability in TES atmospheric observations of Mars during 1999–2003, *Icarus*, *167*, 148–165.

Snyder, C. W. (1979), The planet Mars as seen at the end of the Viking mission, *J. Geophys. Res.*, *84*, 8487–8519.

Sprague, A. L., W. V. Boynton, K. E. Kerry, D. M. Janes, D. M. Hunten, K. J. Kim, R. C. Reedy, and A. E. Metzger (2004), Mars' South Polar Ar enhancement: A tracer for South Polar seasonal meridional mixing, *Science*, *306*, 1364–1367.

Sprague, A. L., W. V. Boynton, K. E. Kerry, D. M. Janes, N. J. Kelly, M. K. Crombie, S. M. Nelli, J. R. Murphy, R. C. Reedy, and A. E. Metzger (2007), Mars' atmospheric argon: Tracer for understanding Martian atmospheric circulation and dynamics, *J. Geophys. Res.*, *112*, E03S02, doi:10.1029/2005JE002597.

Suarez, M. J., and L. L. Takacs (1995), *Technical Report Series on Global Modeling and Data Assimilation: Volume 5: Documentation of the AIRES/GEOS Dynamical Core, Version 2*, NASA Tech. Memo., NASA TM-104606.

Tillman, J. E. (1988), Mars global atmospheric oscillations: Annually synchronized, transient normal mode oscillations and the triggering of global dust storms, *J. Geophys. Res.*, *93*, 9433–9451.

Weiss, B. P., and A. P. Ingersoll (2000), Cold spots in the Martian Polar Regions: Evidence of carbon dioxide depletion?, *Icarus*, *144*, 432–435.

W. V. Boynton, D. M. Janes, K. E. Kerry, and A. L. Sprague, Lunar and Planetary Laboratory, University of Arizona, Tucson, AZ 85721, USA. (wboynton@lpl.arizona.edu; buck@lpl.arizona.edu; krisk@lpl.arizona.edu; sprague@lpl.arizona.edu)

A. E. Metzger, Jet Propulsion Laboratory, 4800 Oak Grove Drive, Pasadena, CA 91103, USA. (albert.e.metzger@jpl.nasa.gov)

J. R. Murphy, Department of Astronomy, New Mexico State University, Las Cruces, NM 88003, USA. (murphy@nmsu.edu)

S. M. Nelli, Department of Atmospheric, Oceanic, and Space Sciences, University of Michigan, Space Science Research Building, 2455 Hayward Street, Ann Arbor, MI 48109, USA. (snelli@umich.edu)